A review on design modalities of solar-pumped solid-state laser

Sonam Berwal [a,b,*], Neha Khatri [a,b], Daewook Kim [c,d]

[a] *Academy of Scientific & Innovative Research (AcSIR), CSIR-CSIO, Chandigarh 160030, India*
[b] *Department of Manufacturing Science & Instrumentation, CSIR-CSIO, Chandigarh 160030, India*
[c] *Wyant College of Optical Sciences, University of Arizona, 1630 E. University Blvd., Tucson, Arizona 85721, USA*
[d] *Department of Astronomy and Steward Observatory, University of Arizona, 933 N. Cherry Ave., Tucson, Arizona 85721, USA*

ABSTRACT

The rapid exhaustion of conventional energy sources and global environmental concerns are opening new opportunities to utilize sustainable and renewable energy. Amid the various renewable sources, solar energy is a promising, inexhaustible, and abundant form of freely available energy. The solar-driven laser system is one of the most acceptable technologies to harness solar power. Solar-powered laser converts the broadband solar radiation directly into the monochromatic, collimated, and coherent laser beam. The emitted laser beam may be widely used in space and terrestrial applications, including free-space optical communication, renewable energy cycle, asteroid deflection, space debris removal, material processing, nano-material production, and electric vehicles. The paper starts with a discussion of solar-powered lasers with distinct gain mediums such as liquid, gas, and solid. This paper illustrates details about the solar-powered solid-state lasers, which have the advantage of inherent high energy density and compactness, relatively low pumping threshold, and potential for efficient solar to laser power conversion. A comprehensive review of solid-state solar laser's construction, working principle, energy conversion process, and beam shaping are also presented. The state-of-the-art procedures have been summarized for laser collection efficiency and laser output power. The power density of solar radiations received on the earth's surface is low and insufficient for lasing action. Hence, the solar concentrators are described in detail to enhance the energy density. Furthermore, the different Nd: YAG laser rods and pumping schemes are explained to reduce the thermal lens effect. Finally, the review is concluded with a conclusion and perspectives.

1. Introduction

Energy is vital for the development and existence of humankind. Over the last few decades, the scientific community found alternative energy resources to reduce the dependency on fossil fuels (oil, coal, gas). Non-renewable energy sources release harmful gases that lead to climate change and enhance the greenhouse effect. The research institutes, industries, and governments are making continuous efforts to adopt renewable sources (wind, hydro, solar, and biomass) to reduce the rapidly aggravating global warming pace.

In the midst of various renewable sources, solar energy is the most generous and can serve as a sustainable source. Society has long recognized the advantage of solar technologies in multiple fields [1–7]. Fig. 1 represents solar technologies, including solar desalination, solar cooking, solar-powered car, solar furnace, solar-powered laser, solar water heater, cabinet solar dryer, solar power plant, etc. Despite this,

solar energy is an abundant form of free energy received on the Earth. The sun provides 1.7×10^{22} J of energy in 1.5 days [8]. This energy is equivalent to all of the energy supplied by the Earth's total oil resources of 3 trillion barrels. The energy received by our planet in one hour from the sun is more than all humans consume in an entire year [9]. Thus, only a tiny part of humankind's energy requirements is fulfilled by solar energy. It now seems that the deployment of an optical system operated directly by sun radiation could make remarkable progress in the continuous acquisition of solar energy technologies.

In recent years, solar-pumped lasers (solar-powered lasers, solar lasers) have shown a tremendous evolution in providing additional value for solar energy consumption. Solar-pumped lasers originated from solar energy and laser physics. The solar-pumped lasers are of interest for space and terrestrial applications, which convert the broadband solar radiation directly into the coherent, collimated, and monochromatic laser beam [17]. Fig. 2 illustrates the opportunity for a wide range of

applications associated with solar-powered lasers.

Owing to the availability of solar radiation for a longer duration and the absence of diffusing atmosphere, the collection rate of solar radiation is higher in space than on the earth. The solar laser in space is more convenient for many environmental and economic benefits. Accordingly, the space-based laser systems would be a breakthrough in technology advancement to fulfil all the energy needs on the earth. Among the transmission of power over the vast distance of approximately 400 kilometres from space to the surface of the earth, the solar lasers are also used in free-space optical communication [18], asteroid deflection [19], space debris removal [20], and for remote sensing from space. Solar lasers for terrestrial applications are equally beneficial to descend the use of coal, oil, and gases. Hence, the solar-powered laser also has immense potential for renewable energy cycle [21], material processing, nano-material production [22], and electric vehicles [23].

This research article reviews and synthesises the various solar-powered solid-state laser approaches used over the past five decades. The development of the solar-powered system is motivated by the clear opportunity to enable solar energy across various implementations from space to earth. This article is broadly classified into four sections. The first section begins with solar-pumped lasers and their types, including gas, liquid and solid. The different solid-state materials are studied to discern the advantage of solid-state Nd: YAG lasers. The second section examines the construction, working, energy mechanism, beam shaping, and historical highlights of solar-powered lasers. After the realization of the importance of collection efficiency and output of lasers, the third section explains the solar concentrators with primary, secondary, and tertiary types. The last section describes the Nd: YAG laser rods with different pumping configurations.

2. Solar-pumped lasers

The solar-pumped lasers came into appearance after discovering the first laser in the year 1960 [24]. Solar lasers express the same optical property as conventional lasers by emitting a collimated laser beam. However, solar-pumped lasers are more reliable, less costly, and much simpler in construction because of the complete removal of electrical power [25]. In electrically driven lasers, the solar energy is initially converted into electricity, and then electrical energy is fed into the laser to generate the coherent beam. Compared with the electrically powered laser, the solar-powered laser saves the two energy conversion steps, as illustrated in Fig. 3.

The astonishing early entry of solar-pumped laser using the sun as a pumping source came in 1963 [26]. Kiss et al. developed the first solar laser by employing calcium fluoride crystal doped with divalent dysprosium (CaF_2: Dy^{2+}) at liquid neon (Ne) temperature (27° K). After a short duration, rapid progress has occurred in solar laser by pumping the liquid [27–29], gaseous [30–35], and solid [17,22,24] active medium through the sunlight. This section describes the solar lasers based on the different active mediums.

2.1. Solar-pumped liquid laser

The first solar-pumped liquid laser was presented in the 1980s. The dye (liquid solution) is employed as a gain medium in solar-powered liquid lasers. Numerous laser mediums are used in the liquid lasers, including phosphorus oxychloride and selenium oxychloride. However, phosphorus oxychloride is more preferred solvent due to less corrosive and less toxic [27].

In 1983, NASA presented a report on a solar-pumped liquid laser for space applications. Schneider et al. used the aprotic solution as an active medium by dissolving the neodymium trifluoroacetate in phosphorus oxychloride with the aid of zirconium tetrachloride ($POCl_3$: Nd^{3+}: $ZrCl_4$) [27]. The advantage of an aprotic solution is that it does provide good stability and improved intrinsic efficiency against decomposition. Seregin et al. developed a pulsed solar-pumped liquid space borne laser utilizing neodymium containing phosphorus oxychloride ($POCl_3$: $SnCl_4$: Nd^{3+}) liquid that provides high output power [28]. This liquid active medium confers the advantage of a lower absorption coefficient at lasing wavelength of 1052 nm. In 2016, Payziyev et al. simulated the solar-powered liquid lasers for enhancing the solar to laser power conversion efficiency by using the neodymium containing phosphorus oxychloride liquid as an active medium [29]. Additionally, the proposed system contains a frequency converter for shifting the part of the solar spectrum that the laser medium does not absorb.

Fig. 1. The utilize of solar technologies in the several fields include, but not limited to the (a) solar desalination [10], (b) solar cooking [11], (c) solar-powered car [12], (d) solar furnace [13], (e) solar-powered laser [14], (f) solar water heater [15], (g) cabinet solar dryer, (h) solar power plant [16].

2.2. Solar-pumped gas laser

A solar-pumped laser in the gaseous state is responsible for obtaining high power due to a large excitation volume [30]. Among the wide range of scientific interests, the investigation of solar-powered gas lasers started in the 1970s [31].

In 1978, a new approach was proposed to pump the gas lasers via an intermediate blackbody [31]. Christiansen presented the idea of pumping infrared molecules via an intermediate blackbody cavity. The blackbody cavity is heated up by the focused solar radiations that energize the laser medium. After one year, Yesil and Christiansen moved a step forward towards more utilization of solar radiation by demonstrating the conception of blackbody radiation pumping of carbon dioxide (CO_2) gas laser [32]. To illustrate the given concept, an experiment is conducted in which a gas mixture (CO_2 - He) is exposed to 1500 k thermal radiation. The experimental value of optical gain with a maximum gain coefficient is $2.8 \times 10^{-3} cm^{-1}$.

In a similar direction, Le and Weaver accomplished the requirement for space deployment from the first atomic iodine solar-pumped gas laser [33]. The proposed system is pumped by simulated solar insolation and enhances the output power by up to 4 W. Subsequently, Insiuk et al. performed the blackbody-pumped CO_2 laser experiment in the year 1984. They experimentally proved the performance of blackbody-pumped gas lasers with an output power of 4.5 mW [34]. In recent years, Danilov et al. presented the experimental and theoretical study of oxygen-iodine laser (OIL). The OIL system is pumped with various methods, including solar pumping. However, the pumping of molecular oxygen from solar radiation is beneficial in overcoming the weight of the space system [35].
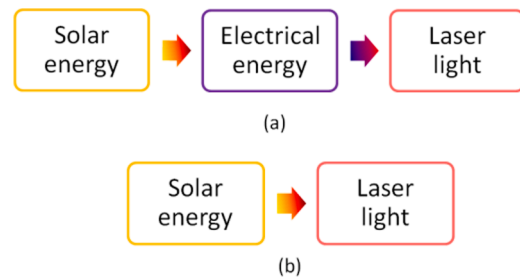

Fig. 3. Energy conversion in (a) Electrical pumped lasers, (b) Solar-pumped lasers.

2.3. Solar-pumped solid-state laser

A solar-pumped solid-state laser utilizes a crystal or glass as the laser medium. The majority of solid-state lasers emit the output beam in the spectral region of 400 nm to 3000 nm [36]. The solid-state laser system can serve as a three-level or four-level based on the specific laser material. Solid-state solar lasers employed different crystals as laser materials, including Nd: YAG, Cr: Nd: YAG, Ce: Nd: YAG, Nd: Cr: GSGG and alexandrite. The selection of a suitable material is necessary to increase the output power of the laser system. Hence, the selected crystal for laser operation must possess a strong absorption band, sharp fluorescent lines, and high quantum efficiency [36]. The description of crystals for solar-pumped solid-state lasers is given below
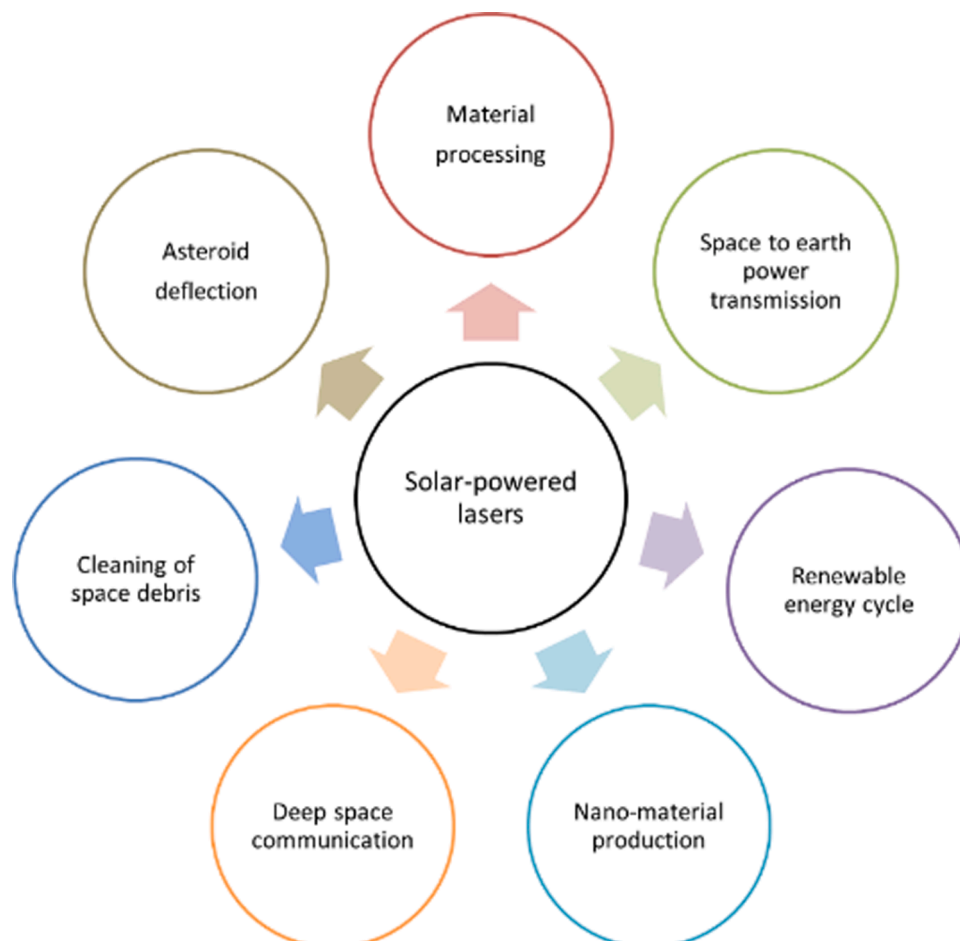

Fig. 2. The possible applications of solar-powered lasers.

2.3.1. Nd: YAG

Neodymium doped yttrium aluminium garnet (Nd: YAG) is the most prevalent laser material for solid-state lasers [17,22,37-39]. Nd: YAG material owns the unique characteristics that make it favourable for laser operation. The host material (YAG) is hard and has high thermal conductivity. Moreover, the cubic structure of YAG approval a narrow fluorescent linewidth that results in a low threshold and high gain for laser operation. The optical and physical properties of Nd: YAG are listed in Table 1.

Fig. 4 illustrates the four-level energy diagram of Nd: YAG laser material. The solid-state Nd: YAG laser is a four-level system except at the wavelength of 946 nm. The advantage of a four-level laser system is that the population inversion is attained easier than the three-level systems. The lower level of a four-level system is much above the ground state and rapidly depopulated by multi-photon transitions. Due to this, the reabsorption can be averted, and a lower threshold pump power can be attained, making it easy to acquire stimulated emission. The emission wavelengths for Nd: YAG laser are 946, 1064, 1123, and 1319 nm [36].

However, the highest gain is achieved at the wavelength of 1064 nm. At 946 nm, the Nd: YAG laser works as a quasi-three-level system requiring higher pump intensity than four-level systems. At the wavelength of 1123 nm, laser operation is very challenging to obtain because of weak transition.

Owing to the broadband pump absorption and four-level characteristics of Nd: YAG material, it can be used efficiently for solar lasers. However, the overlap between the Nd: YAG absorption spectrum and solar emission spectrum is small [43]. Nevertheless, in comparison with other, Nd: YAG is the best material under highly concentrated solar radiation due to its high quantum efficiency and excellent thermal conductivity. The first solar laser using Nd: YAG crystal was developed by C G Young, which uses direct solar radiations for pumping [37].

2.3.2. Cr: Nd: YAG

The main concern for solar-pumped lasers is the efficiency of transferring energy from the pump source to the laser crystal. After the Nd: YAG solar laser, significant efforts have been made to enhance the absorption of solar radiation in laser medium. In recent years, to improve the performance of Nd: YAG laser, chromium co-doped (Cr: Nd: YAG) Nd: YAG ceramics materials have attracted more attention [44–47].

In the visible region, the sensitizer Cr^{3+} ions have broad absorption bands [48]. The critical observation is that doping of Cr^{3+} ions in an Nd: YAG crystal considerably increases the absorption of solar radiations in the visible spectrum [49,50]. Fig. 5 illustrates the energy level diagram of Cr^{3+} and Nd^{3+} ions in YAG crystal. After the pump light absorption, Cr^{3+} ions get excited to the $^4T_2$ state or ^2E state. By the transitions of Cr^{3+} ions from excited states ($^4T_2$ or ^2E) to the ground state ($^4A_2$), it is believed that energy is transferred from Cr^{3+} to Nd^{3+} ions to put Nd^{3+} ions eventually into the metastable excited state ($^4F_{3/2}$) [51]. The transfer of energy from Cr^{3+} to Nd^{3+} increases the pumping efficiency and decreases the threshold power for laser oscillation [51].

In the case of single-shot laser operation, the Cr: Nd: YAG efficiency becomes more than double that of the Nd^{3+}: YAG ceramic rod [25]. At low repetition rates, the average output power of Cr: Nd: YAG laser rod is higher than that of Nd: YAG [25].

The Cr: Nd: YAG laser medium was initiated by Yabe et al. in 2007 to improve the performance of solar-powered lasers [22]. However, the preliminary investigation revealed that the performance of Cr: Nd: YAG ceramic is inferior to that of Nd: YAG crystals because of the increased scattering coefficient of the rods that led to an increase in the round-trip loss in the laser cavity [21]. Further, the research community have appreciably enhanced solar lasers' collection and slope efficiencies by employing Cr: Nd: YAG laser rods [52,53]. In 2018, Liang et al. reported significant progress in solar laser by employing a Cr: Nd: YAG laser rod with an enhanced collection efficiency of 32.5 W/m^2 and 6.7% slope efficiency [53]. The obtained slope efficiency from Cr: Nd: YAG rod is 1.28 times better than that of the previous Nd: YAG laser rod [54].

2.3.3. Ce: Nd: YAG

The co-doping of cerium (Ce^{3+}) ions in Nd: YAG crystal is a promising method for enhancing the laser efficiency of solar-pumped lasers. The spectrum of Ce^{3+} in YAG lies in the strongest region of solar spectrum. Since 1969, continuous efforts have been made to co-doping the Nd: YAG crystal with a sensitizer element Ce^{3+} under broadband pumping [55]. Mares and the group studied the energy transfer mechanism between Ce^{3+} and Nd^{3+} at low temperature (T = 4.4 K) [56]. In 2015, Tai et al. presented a mechanism based on the energy transfer of Ce^{3+} and Nd^{3+} in YAG [57]. The obtained results indicated that Nd^{3+} emissions located at 1064 nm is efficiently enhanced with Nd^{3+} concentration because of energy transfer from Ce^{3+} [57].

Accordingly, the co-doping of Nd: YAG laser medium with cerium ions can improve the laser efficiency significantly due to broader and strong absorption bands in the ultraviolet (UV) and visible spectral regions [56–58]. The absorption spectrum of the Ce: Nd: YAG has two broad absorption bands centered at 339 nm and 460 nm that are characteristic of the Ce^{3+} ion in YAG lattice and additional bands (red and near-infrared regions) that correspond to the absorption spectrum by Nd^{3+} ions in YAG structure [59]. The energy level diagram of Ce: Nd: YAG laser medium is illustrated in Fig. 6. After absorption of the pump photon, the Ce^{3+} ions get excited from the ground state ($^2F_{5/2}$) to the d shell (5d$_2$ ($^2B_{1g}$) and 5d$_1$ ($^2A_{1g}$)) of the Ce^{3+} ions. After the short duration, the excited electrons decay non-radiatively to the lower pump band (5d$_1$) and further decay radiatively to the ground state ($^2F_{5/2}$). Hence, a radiative transfer mechanism takes place via a cross-relaxation process between the 5d$_1$ ($^2A_{1g}$) → $^2F_{5/2}$ for Ce^{3+} ions and $4I_{9/2}$ → $^2G_{7/2}$ transitions of Nd^{3+} ions, as shown in Fig. 6 indicated by pathway (1) via the cross-relaxation process [57].

The second energy transfer process occurs based on a quantum cutting down-conversion process [57], as represented by pathway (2) in Fig. 6. This mechanism implies that two near-infrared (NIR) photons can emerge from a single absorbed visible (VIS) photon since the energy of the transition 5d$_1$ ($^2A_{1g}$) → $^2F_{5/2}$ of the Ce^{3+} ion is almost twice as high as the energy difference between the $^4F_{3/2}$ and $^4I_{11/2}$ levels of the Nd^{3+} ion [57,60].

In solar-pumped lasers, the first study of Ce: Nd: YAG laser system based on simulations was accomplished by Payziyev and the group in the year 2018 [50]. The simulated model of laser system revealed that a slope efficiency and output power of the Ce: Nd: YAG solar-pumped laser

Table 1
Properties of Nd: YAG material [36].

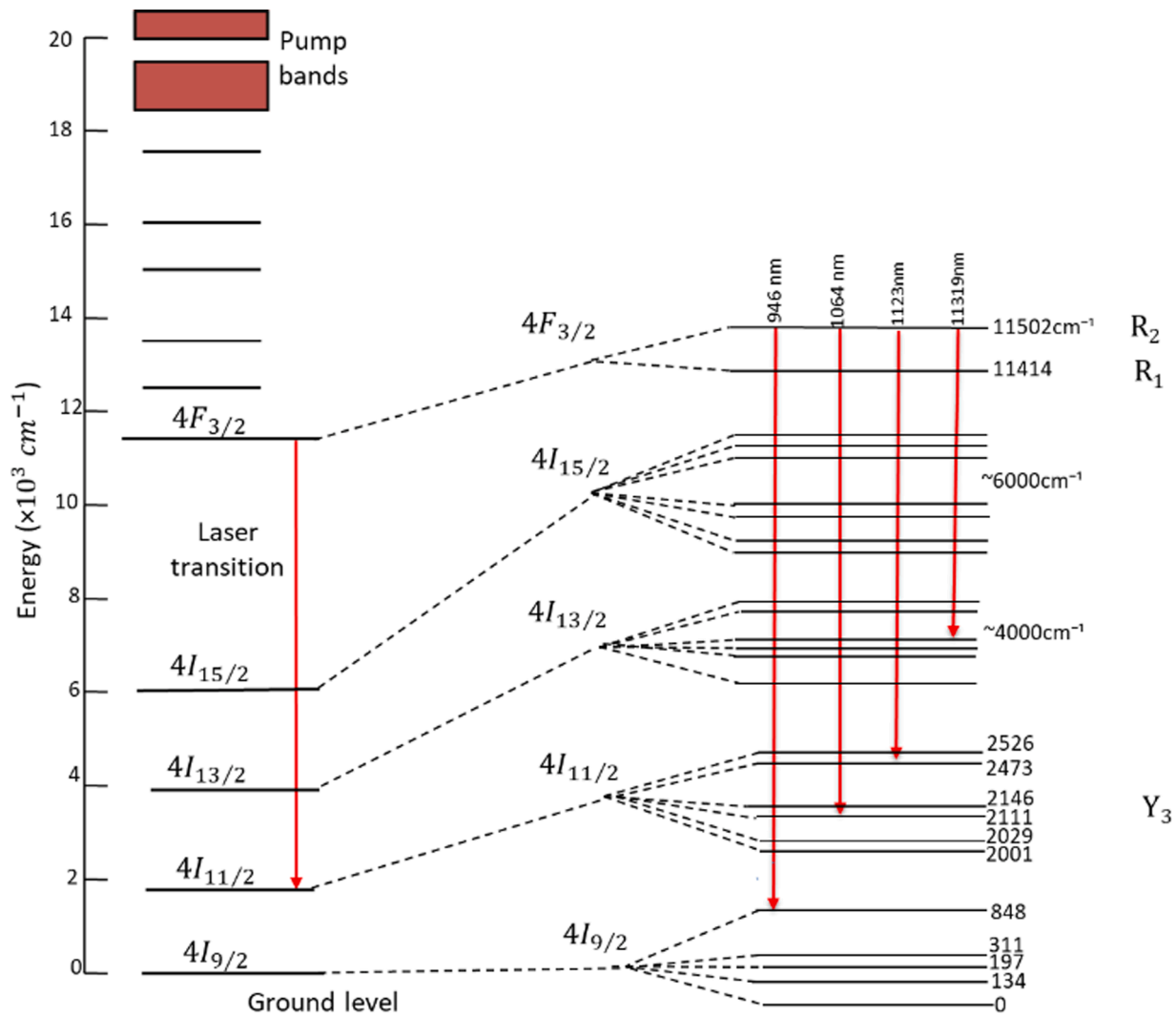| Chemical formula	Nd: $Y_3Al_5O_{12}$
Weight % Nd	0.725
Atomic % Nd	1.0
Melting point	1970 °C
Density	4.56 g/cm^3
Knoop hardness	1215
Index of refraction	1.82
Modulus of elasticity	3×10^3 kg/cm^2
Photon energy at 1060 nm	1.8610
Nd atoms/cm^3	1.38×10^{20}
Fluorescence lifetime	230 μs
Line width	120 GHz
Rupture stress	$1.3\text{-}2.6 \times 10^3$ kg/cm^3
Tensile strength	200 MPa
Scatter losses	0.002 cm^{-1}
Stimulated emission cross section	
$R_2 - Y_3$	$\sigma_{21} = 6.5 \times 10^{-19}$ cm^2
$^4F_{3/2} - {}^4I_{11/2}$	$\sigma_{21} = 2.8 \times 10^{-19}$ cm^2
Thermal expansion coefficient	
[40] orientation	8.2×10^{-6} C^{-1}, 0-250 C
[41] orientation	7.7×10^{-6} C^{-1}, 10-250 C
[42] orientation	7.8×10^{-6} C^{-1}, 0-250 C
Thermal conductivity	14 W/m.K
Fracture strength	180-210 N/mm^2

Fig. 4. Energy level diagram of Nd: YAG laser material [36].

is increased by a factor of two as compared to the Nd: YAG laser. However, the experimental analysis of solar-pumped Ce: Nd: YAG lasers is still in initial stages. The first experimental-based evaluation of solar-pumped laser by employing the Ce: Nd: YAG as a laser medium is conducted by Vistas et al. in 2020 [61]. In respect of Nd: YAG solar-pumped laser, the collection efficiency of the end-side-pumped solar Ce: Nd: YAG laser is reduced by nearly half (4.9 W/m^2) due to the larger scattering loss within the crystal. In year 2021, again Vistas et al. conducted an experimental evaluation of Ce: Nd: YAG gain medium with a side-pumped configuration of solar-powered laser [62]. The obtained result shows that the collection efficiency was 1.57 times better than that of the Nd: YAG solar-powered laser [62]. After a comparison of Ce: Nd: YAG end-side-pumped solar laser with the Ce: Nd: YAG side-pumped configuration, it is declared that the collection efficiency, slope efficiency, and solar-to-laser power conversion efficiency of the proposed system are 4.82, 4.00, and 4.67 times higher, respectively [62]. In 2022, Liang et al. proposed a most efficient simultaneous solar laser emissions from three Ce: Nd: YAG rods within a single pump cavity [63]. From the 356 W of incoming solar power, the laser system produced 16.5 W of CW multimode solar laser power, corresponding to a 4.64 % solar-to-laser conversion efficiency, 41.25 W/m^2 collection efficiency, and 7.64 % slope efficiency [63]. In recent, Almeida and the group developed a CW side-pumped Ce: Nd: YAG solar laser with the highest laser output of 40 W [64].

2.3.4. Nd: Cr: GSGG

Neodymium and chromium co-doped gadolinium scandium gallium garnet (GSGG) has appeared as an essential crystalline laser host material. In the year 1976, GSGG with trivalent neodymium (Nd^{3+}) was employed as laser material [65]. Nd: Cr: GSGG is advanced to possess high efficiency and low threshold for pumping solar lasers [48,66–68]. The co-doping of GSGG with Cr and Nd presents the strong absorption of solar radiation but, at the same time, increases the heat in the crystal [67]. The thermal conductivity of Nd and Cr co-doped GSGG is around 2.5 times less than Nd: YAG. Hence Nd: Cr: GSGG crystals are hard to operate under highly intense solar radiations because of their lower thermal conductivity and small fracture resistance [36].

In 2007, Endo proposed a conical-toroidal resonator combined with Nd/Cr co-doped GSGG thin disk for space-based solar-pumped solid-state lasers. Endo declared that the suggested system is convenient for solar pumping, and the pump source can irradiate the broad disk efficiently [68].

2.3.5. Alexandrite

Alexandrite (BeAl$_2$O$_4$: Cr^{3+}) is used for high power operations because of its good thermomechanical properties. The crystal is optically and mechanically alike to ruby. The thermal conductivity of alexandrite is 23W/m.K, which is almost twice of Nd: YAG material and two-thirds of the ruby. The fraction resistance of alexandrite is five times that of Nd: YAG [36]. The broad emission bands of alexandrite in the visible
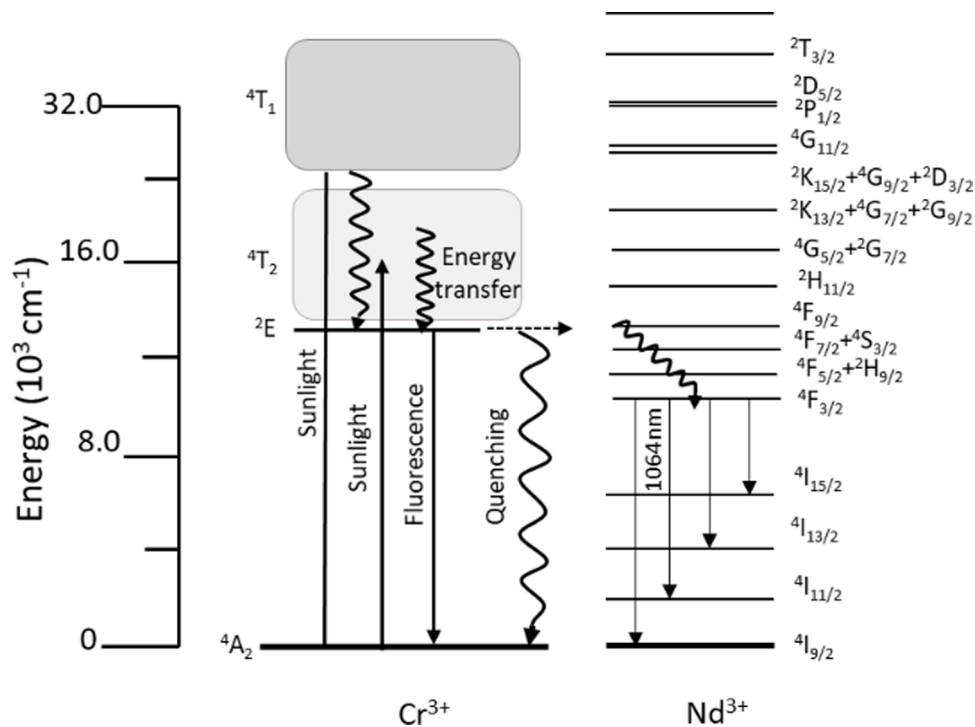
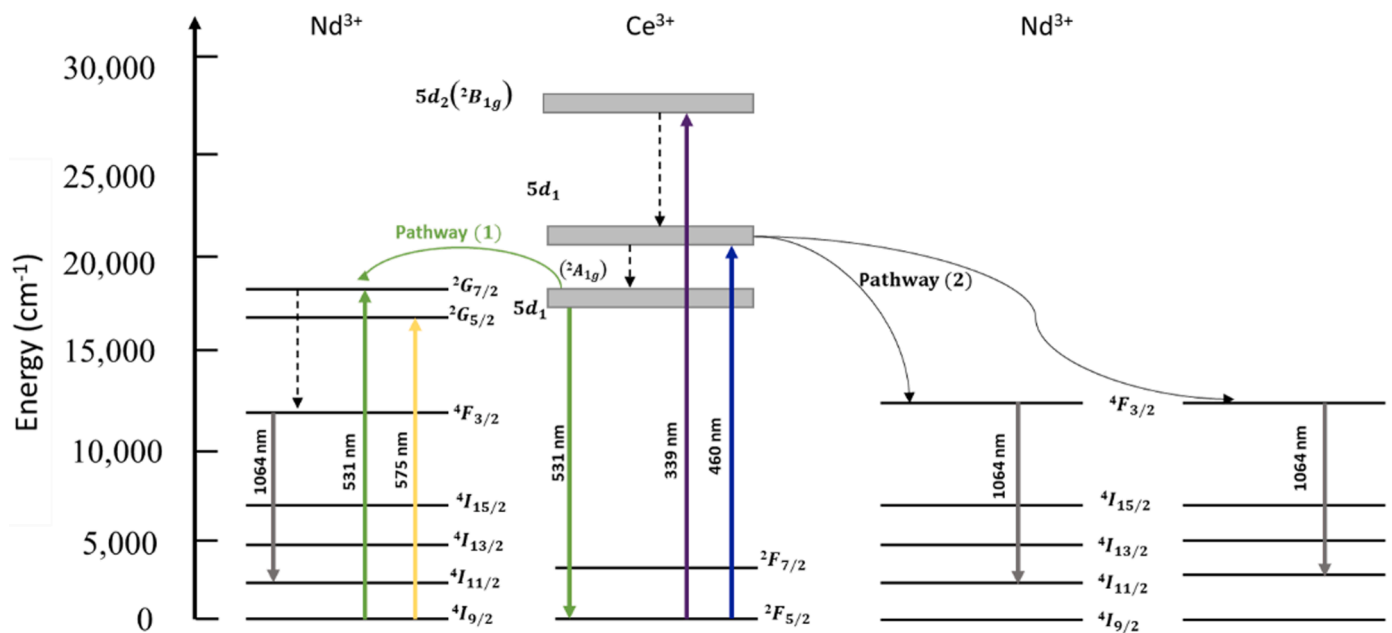**Fig. 5.** Energy level diagram of Cr: Nd: YAG laser material [51].

Fig. 6. Energy level diagram of Ce: Nd: YAG laser material [57,59].

spectrum enable various pump sources, such as flash lamps, mercury and xenon lamps, and natural sunlight. Only a few studies on solid-state alexandrite lasers have appeared. Lando et al. developed the first solar-pumped alexandrite laser in 1999 [47]. Alexandrite crystal has broadband absorption for solar radiations in the visible range, but laser action needs a high threshold pump intensity, which is a real challenge [44,47,66].

3. Overview of solar-powered solid-state lasers

Solid-state lasers are prominent among the gas and liquid lasers due

to their inherent high energy density and compactness, relatively low pumping threshold, and feasibility for efficient solar to laser power conversion [66]. The prime factor that affects the choice of Nd: YAG material is its suitable mechanical and thermal properties, which makes it durable and resilient. This section reviews the solar-powered solid-state laser in detail with construction, working, energy conversion process, beam shaping, and history of developed systems.

3.1. Construction

The solar-powered solid-state Nd: YAG laser is fundamentally

categorized into four parts such as pump source, solar concentrator, laser medium, and an optical resonator, as shown in Fig. 7. The pump source supplies energy to achieve population inversion that causes laser light emission. The sun acts as a pump source in solar lasers, and solar radiations provide energy to the laser medium. However, the sun is farther (147.7 million km) from the laser head, and hence the lasing action is more complicated to attain.

On sunny days, solar radiation has a power density of 1000 W/m^2 at the terrestrial surface. However, solar radiation must be extremely concentrated to surpass the lasing threshold. Accordingly, some collectors are needed to collect and concentrate low-density solar radiation. A typical solar laser utilizes various solar concentrators, such as primary, secondary and tertiary, to achieve enough pumping intensity for the lasing threshold. Primary concentrators collect and concentrate the solar radiation to a focal zone, where a solar laser head is introduced. Secondary concentrators are employed to concentrate and distribute the solar radiations from the focal zone of the primary concentrator to the laser-active medium. Tertiary concentrators are also indispensable for high-flux pumping of the laser medium since they can compress the concentrated solar radiations from their input aperture to the laser-active medium.

The active medium (laser medium, gain medium) of solar-powered Nd: YAG lasers comprise a rod of synthetic crystalline material (yttrium aluminium garnet) doped with neodymium. Due to the high intensity of focused sunlight on the laser medium, electrons from the lower energy state get excited and move to the higher energy state, causing laser action to occur. The cerium and chromium co-doped Nd: YAG materials are also utilized for lasing action. The doping of Cr^{3+} and Ce^{3+} ions in an Nd: YAG crystal considerably increases the absorption of solar radiation.

The laser resonator (laser resonant cavity, optical resonator) is the most crucial part of the solar laser that encloses the active medium and provides feedback to the laser light. The laser resonator combines two mirrors in which the Nd: YAG rod is emplaced. At the primary end of the rod, the mirror is fully reflective, completely reflecting the light. The second end is partially reflective, reflecting most light and allowing some light to pass through to produce a laser beam. Apart from these parts of solar-powered lasers, the cavity shape and coolant are also considered essential for solar lasers. To confine the light inside the cavity, the perfect shape of the cavity is necessary. Based on the previous research, the cavity's shape can be conical, compound V-shaped, etc. [17,22]. The coolant is requisite for removing the generated heat inside the laser cavity. The cooling water helps prevent the laser rod from IR heating and UV solarization.

3.2. Working

The emitted beam from the laser (light amplification by stimulated emission of radiation) is distinguishable from ordinary light sources. In order to acknowledge the operating principle of laser, it is necessary to establish how the process of stimulated emission can give rise to light amplification [69]. In 1917, Albert Einstein developed the framework for the amplification of EM (electromagnetic) radiations by stimulated emission [70].

The working of a laser depends on the interaction of light and matter. The atoms, ions, and molecules exist only in discrete energy states. The change of energy from one state to another is known as a transition [36]. The transition is concerned with either absorption or emission of a photon. The wavelength of the emitted or absorbed radiations is specified from Bohr's frequency relation [71,72] as given in Eq. 1

$$\Delta E \ = E_2 \ - E_1 = h\nu_{21} \tag{1}$$

where E_1 and E_2 are two discrete energy levels, but $E_2 > E_1$, h is Planck's constant (6.626×10^{-34} J.s), and ν_{21} is the frequency.

A solid-state material is an ensemble of many similar atoms. When an extensive collection of identical atoms is in thermal equilibrium at temperature T, the relative populations of any two energy levels (E_1 and E_2) must be related by the Boltzmann ratio as expressed by Eq. 2 [71]

$$\frac{N_2}{N_1} = \frac{g_2}{g_1}\frac{N_2'}{N_1'} = \frac{g_2}{g_1}\exp\left(\frac{-(E2 - E1)}{kT}\right) \tag{2}$$

where N_1 and N_2 are the numbers of atoms in relative energy levels, k is the Boltzmann constant, T is temperature, and g is degenerate. The term "degenerate" refers to when two or more states have the same energy level.

The solid-state Nd: YAG laser is a four-level system and involves four energy levels (E_1, E_2, E_3, and E_4). Fig. 8 demonstrates the Nd: YAG laser action, causing population inversion in which the higher energy state is more populated than the ground-state state. At thermal equilibrium, the numbers of atoms are more in the lower energy state (E_1) than in the higher energy states (E_2, E_3, E_4). When the highly concentrated solar radiation interacts with the laser medium, the ions or molecules get excited from a lower energy state to a higher energy state. This process is known as absorption, in which the population of the lower level (N_1) will be depleted at a rate proportional to $\rho(\nu)$ (radiation density). The population of that level is given by Eq. 3 [36].

$$\frac{\partial N_1}{\partial t} \ = \ -B_{12} \ \rho(\nu)N_1 \tag{3}$$

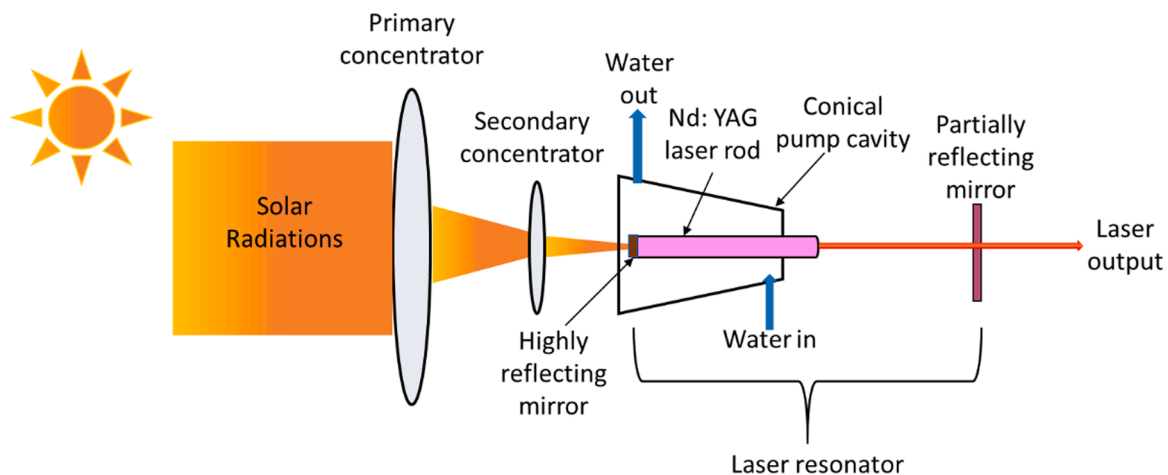After the absorption of a photon, an atom is excited into a high-

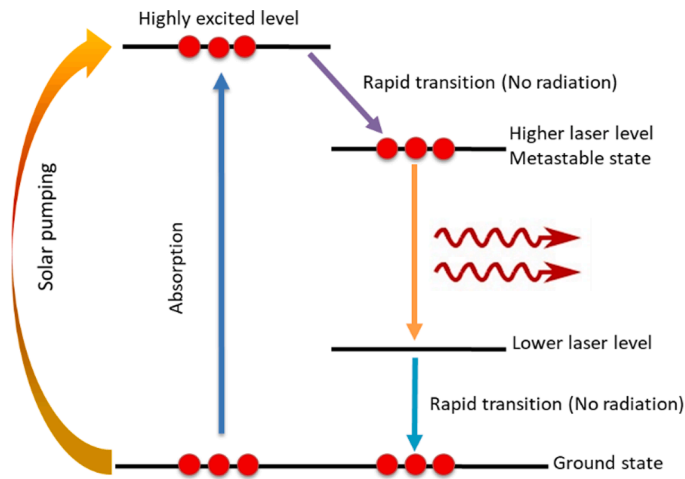**Fig. 7.** Schematic diagram of solar-powered solid-state Nd: YAG laser.

Fig. 8. Lasing action of four-level solid-state Nd: YAG laser.

energy state. However, after a short duration, it returns to the intermediate state by releasing energy in the form of a photon. The released photon carries the energy in a random direction. This process is called spontaneous emission, in which the population of the upper level decays spontaneously to the lower level at a rate proportional to the upper-level population [36]. The process of spontaneous emission is shown in the following Eq. 4

$$\frac{\partial N_2}{\partial t} = -A_{21}N_2 \tag{4}$$

where the minus sign indicates that the time derivative is negative and A_{21} is a constant of proportionality with dimensions s^{-1}. Compared to stimulated emission, spontaneous emission occurs in the absence of an electromagnetic field, where the emitted quanta are incoherent [36]. Hence, the A_{21} Einstein coefficient is a loss term and instigates into the system photons that do not phase related incident photon flux of the electric field.

The basis of laser action relies on the absorption and emission of radiation processes. During the spontaneous emission process, an atom absorbs energy and gets excited, and this excited state decays spontaneously by re-emitting a photon. The re-emitted photon comes across another atom in the excited state that has not yet decayed spontaneously. The incident photon causes the excited atom to decay before it would have decayed spontaneously. Hence, the incident photon and the photon from the stimulated emission are in phase, indistinguishable, and have the same polarization vector [36]. Therefore, these factors are responsible for the high degree of coherence that characterizes the emission from the laser. In the stimulated emission, the population of the higher energy level (N_2) will be depleted at a rate proportional to the radiation density of the radiation field and the population of the level, as shown in Eq. 5

$$\frac{\partial N_2}{\partial t} = -B_{21} \ \rho(v)N_2 \tag{5}$$

where B_{21} is a constant of proportionality with the same condition as B_{12}. When there is no degeneracy or if the levels have unequal degeneracy, the Einstein coefficients for stimulated emission and absorption are equal ($B_{21} = B_{12}$).

3.3. Energy conversion process

The conversion of energy from solar radiation to the laser beam is also known as energy transformation. The performance of solar-powered lasers depends on the overall system efficiency and output power. The solar laser is built by combining the different optical elements; hence, it

is essential to understand the system design parameters' dependency and interrelationship to enhance overall laser efficiency. Fig. 9 illustrates the energy conversion process of solar-powered solid-state Nd: YAG lasers in four steps [36].

The overall efficiency of solar-powered solid-state Nd: YAG laser is the product of the individual efficiencies [36,66,73–76], including the pump source efficiency (η_P), transfer efficiency (η_T), absorption efficiency (η_A), quantum efficiency (η_Q), stokes efficiency (η_S), beam overlap efficiency (η_B), and extraction efficiency (η_E). The energy that arrived as solar radiations on the earth is firstly converted into useful pump radiations. The useful pump radiation from the sun is only that radiation that falls onto the absorption band of the active medium. Thus, the pump source efficiency is calculated as the fragment of input power (P_{IN}) emitted as optical radiations within the absorption region of the laser medium (P_P), as shown in Eq. 6 [74].

$$\eta_P = \frac{P_P}{P_{IN}} \tag{6}$$

In solar-powered solid-state Nd: YAG laser, the pump source efficiency relies on the overlap of the emission spectrum of solar radiations and the absorption spectrum of Nd: YAG material. The pump power efficiency is also defined as a product of electrical to optical power efficiency and overlap efficiency. However, solar lasers are not powered by electricity, and hence, the pump power efficiency (η_{PSL}) is determined by Eq. 7 [66]

$$\eta_{PSL} = \eta_{OVP} = \frac{\int_{\lambda_1}^{\lambda_2} g_\lambda d\lambda}{\int_0^\infty g_\lambda d\lambda} \tag{7}$$

where the overlapping efficiency (η_{OVP}) for Nd: YAG laser is 0.16 and g_λ is the spectral irradiance of the pumping source. λ_1 and λ_2 represent the wavelength range within the absorption bands of the laser medium.

In the second step, the transfer efficiency of useful pump radiations into the active medium is calculated. However, the transfer efficiency is affected by various factors, including the shape of solar concentrators and pump cavity, the diameter of Nd: YAG rod, absorption losses in optical elements and coolant fluid, and radiation losses through spaces in the laser cavity. The transfer efficiency of solar lasers is calculated by Eq. 8 [74].

$$\eta_T = \frac{P_T}{P_P} \tag{8}$$

Consequently, the pump radiations are primarily absorbed, and then absorbed radiations are transferred to the upper level of the laser medium. The ratio of absorbed power (P_A) to pump power incident on the active medium (P_T) is known as absorption efficiency. In the third step, absorption efficiency is calculated as shown in Eq. 9 [36]

$$\eta_A = \frac{P_A}{P_T} \tag{9}$$

The part of the absorbed pump power emitted at the laser transition (P_U) is defined as the upper state efficiency (η_U). The upper state efficiency is the product of quantum efficiency (η_Q) and quantum defect efficiency (η_S). Quantum efficiency is defined as the ratio of the number of photons contributing to laser emission and the number of pump photons. Solid-state Nd: YAG lasers have a quantum efficiency of 0.9 [36]. The quantum defect efficiency is also known as the stokes factor. As shown in Eq. 10, the Stokes factor is determined as the ratio of photon energy released during the laser transition ($h\upsilon_L$) to the energy of a pump photon ($h\upsilon_P$).

$$\eta_S = \left(\frac{h\vartheta_L}{h\vartheta_P}\right) \tag{10}$$

After that, the upper state energy is converted into the laser output. In the fourth step, the efficiency is divided into two parts; one is the beam overlap efficiency, and the second is the extraction efficiency. The
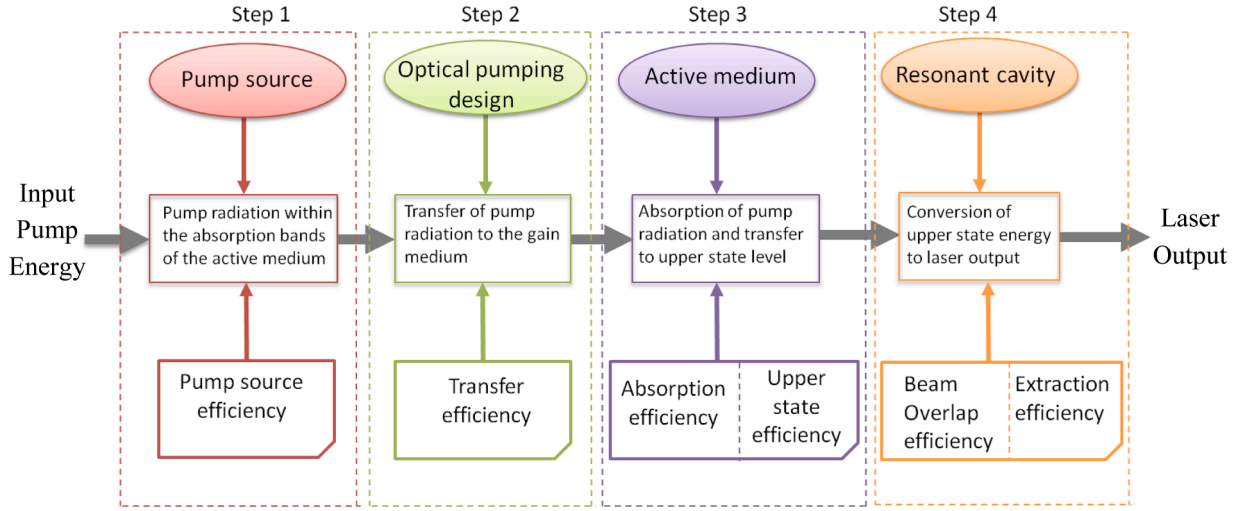
Fig. 9. Four steps energy conversion process for solar-powered Nd: YAG lasers [36].

beam overlap depends on the Nd: YAG rod diameter, optical resonator (radius of curvature of mirrors and cavity length), and pumping methods, while the overlap efficiency is the spatial overlap between the resonator modes and the pump area around the laser medium. The overlap efficiency is calculated as shown in Eq. 11 [74]

$$\eta_B = \frac{\int I_{PM}(r) I_{RM}(r) 2\pi r dr}{\int I_{Rm}^2(r) 2\pi r dr} \quad (11)$$

where I_{PM} is called the absorbed pump intensity distribution, and I_{RM} is known as the resonator mode intensity distribution. The extraction efficiency is expressed as the fraction of total available upper state power as calculated from Eq. 12

$$\eta_E = \frac{P_{OUT}}{P_{Uavail}} \quad (12)$$

During the emission of a laser beam, different losses, including absorption, scattering and diffraction, are present within the active medium. The combination of all three losses generates the round-trip resonant cavity losses [73]. The diffraction loss primarily depends on the radius of curvature of resonator mirrors, resonator length, and rod diameter. However, the diffraction loss is minimal in a large diameter rod within a short resonator. The imperfect coating of resonator cavity mirrors also contributed to the round-trip losses. The reduction of available output power because of losses in the resonator can be calculated from the coupling efficiency (η_C), as shown in Eq. 13

$$\eta_C = \frac{T}{\delta + T} \approx \frac{-\ln R}{\delta - \ln R} \quad (13)$$

where R is the reflectivity and T is the transmission of the output mirror. δ defines the round trip loss as the sum of two-way loss within the laser medium ($2\alpha l$), diffraction losses (δ_D), and absorption and scattering losses at mirrors (δ_M) [17]. The coupling efficiency is directly proportional to the slope of the output versus the input curve of a solar laser. However, the system efficiency is related to the extraction efficiency, as indicated in Eq. 14 [74].

$$\eta_{Slope} = \eta_P \eta_T \eta_A \eta_Q \eta_S \eta_B \eta_C = \eta_P \eta_T \eta_A \eta_Q \eta_S \eta_B \left(\frac{-\ln R}{\delta - \ln R} \right) \quad (14)$$

The slope efficiency is also defined from the Eq. 15

$$\eta_{Slope} = \frac{P_{OUT}}{P_{IN} - P_{TH}} \quad (15)$$

where P_{TH} is the power required to achieve the laser emission threshold. The laser output can be calculated in terms of input pump power as

expressed in Eq. 16 [73].

$$P_{OUT} = (-\ln R) \left(\frac{\eta_P \eta_T \eta_A \eta_Q \eta_S \eta_B}{\delta - \ln R} P_{IN} - A I_s \right) \quad (16)$$

where I_S is the saturation intensity, and A is the cross-section area of the laser rod. The output of solar power lasers can be expressed by Eq. 17, in which pump efficiency is replaced by the overlap efficiency

$$P_{OUT} = (-\ln R) \left(\frac{\eta_{OVP} \eta_T \eta_A \eta_Q \eta_S \eta_B}{\delta - \ln R} P_{focus} - A I_s \right) \quad (17)$$

where P_{focus} represents the collected solar power at the focus. Many researchers used P_{focus} to define the slope efficiency of solar-powered lasers [22,28,38]. Eq. 18 calculates the threshold pump power of the solar laser at the focus [76].

$$P_{TH} = \left(\frac{\delta - \ln R}{\eta_P \eta_T \eta_A \eta_Q \eta_S \eta_B} A I_s \right) \quad (18)$$

The collection efficiency (*CE*) is calculated to determine the performance of solar-powered lasers. The collection efficiency is measured as the ratio of laser output power and the area of the primary solar concentrator, as expressed in Eq. 19 [77].

$$CE = \frac{P_{OUT}}{A_{collection}} \quad (19)$$

3.4. Beam shaping

The beam shaping is a process of redistributing the irradiance and phase of optical radiation [78]. The irradiance distribution determines the beam shape, and the phase of shaped beam is a prime factor for establishing the propagation properties of the beam profile.

The numerous laser applications including materials processing, lithography, medical applications, laser printing, micromachining in the electronics industry, and laboratory research [78,79] required the beam shaping for the use of controlled and uniform light distribution. The beam shaping techniques are broadly classified as apertured beams, beam integrators, and field mapping [80].

In the beam apertured method, beam is expanded and an aperture is employed to select a suitably flat portion. However, the primary drawback of this method is that it frequently results in substantial energy loss. Additionally, it might not be possible to find an aperture size and position that produces the desired outcome if the input beam irradiance is not sufficiently smooth [80]. The beam integrators method is applicable to the low spatial coherence beam where the input beam is divided into the array of beamlets [80]. In the field mapping approach, a phase

element is utilized to map the laser beam into the required profile in a given plane [78].

The beam shape of laser output can be classified as conventional (Gaussian, top-hat) and non-conventional (Bessel, doughnut-shaped) intensity profiles [81] as illustrated in Fig. 10. The most common profile of laser beam is Gaussian and top-hat. To convert the Gaussian energy distribution into the top-hat beam profile, several optical elements such as such as reflective [82], refractive [83], diffractive [84] and freeform lenses [85], and via optical fibers with a modified core [86] are useful. Experimentally, it is not feasible to create an idyllic top hat beam profile with zero energy at its edges and a constant energy distribution along its cross-section; hence, an infinite spatial frequency spectrum is required [78]. The non-conventional beam shapes are required for a specific application that could not be feasible with either Gaussian or top-hat beams. The doughnut-shaped profile (TEM$_{01}$* mode) are essential to increase the laser technology applications, especially at nanoscale, extending laser materials processing techniques, improving lithography accuracy, and creating novel structures in materials [78, 81]. For generation of a doughnut-shaped beam, the spatial light modulators, apertures or inserting additional phase elements in a laser cavity are used [81,87–90].

In 2018, Almedia et al reported the first emission of doughnut-shaped solar laser beam from a side-pumped grooved Nd: YAG rod. The output power of the proposed system is 3W with a long asymmetric laser resonator. The presented laser system does not utilize any additional optical phase element in the resonator [91]; hence, the laser power losses and system complexity becomes reduced. After one year, Vistas and the group improved the output power by 1.67 times higher than the previous record of doughnut-shaped Nd: YAG solar-powered laser using an end-side pumping configuration [92]. In the year 2021, Catela and the group provides a numerical analysis for the formation of doughnut-shaped and top-hat solar laser beams [93]. The authors concluded that the laser rod diameter is a prime factor for generation of laser beam profiles via adopting a symmetrical side pumping technique [93].
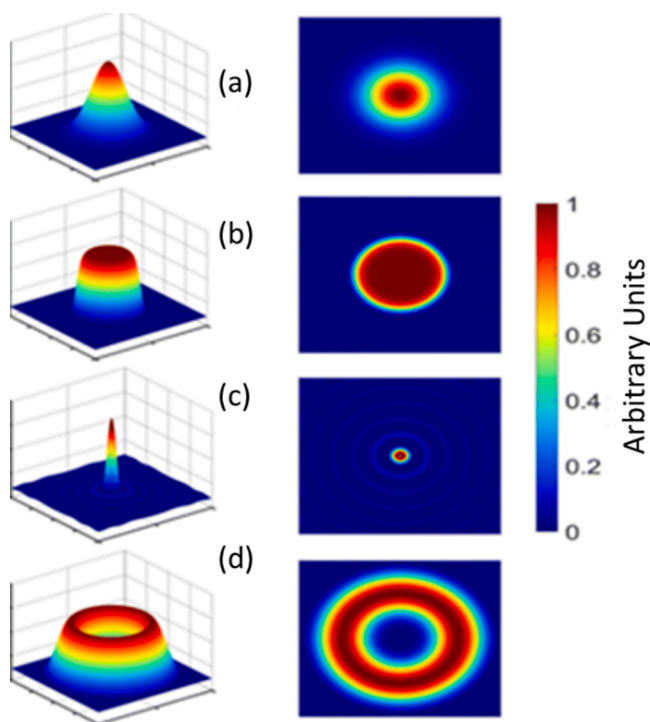

Fig. 10. 2D and 3D intensity distributions of (a) Gaussian beam; (b) Top-hat beam; (c) Bessel beam; (d) annular or doughnut beam [81].

3.5. Historical highlights

The earliest solar-powered Nd: YAG laser was proposed by C G Young, which uses a modified Cassegrain sun-tacking telescope [37]. The telescope consists of three mirrors; the primary is a paraboloidal mirror (61 cm), the secondary is a water-cooled hyperbolic cylindric mirror, and the tertiary is a hemicircular cylindrical mirror. The output power from the proposed solar-powered laser is 1 watt. Young also declared that the developed solar laser system is suitable for space communication. In 1984, Arashi et al. expanded the progress of solar lasers by developing an Nd: YAG laser system using a 10 m aperture of paraboloidal mirror that accounts for the output power of 18 W [38]. This is the highest output power of solar lasers reported by researchers in 18 years. For the assessment of laser performance, they also introduced collection efficiency. However, the obtained collection efficiency from the proposed system is very low. After little progress in the solar-powered Nd: YAG laser research, Weksler et al. designed 600 spherical mirrors and a compound parabolic concentrator (CPC) to enhance the coupling of solar radiations into the laser rod [66]. The obtained output of the solar laser is more than 60 W from the efficient conversion of solar energy, and the slope efficiency exceeds 2%.

In every solar-powered laser, the first challenge is creating a conversion of solar radiations into a laser beam with optimal collection efficiency. Before 1996, there was only a propensity to enhance the output power of solar-powered Nd: YAG laser. However, the most crucial parameter for evaluating laser performance is its collection efficiency, which was not considered gravely.

In the year 1996, Jenkins's approach included Nd: YAG solar laser, side pumped by the high-flux solar furnace (HFSF) that accounts for collection efficiency of 4.7 W/m^2 [94]. The laser system consists the 25 hexagonal segments and a parabolic mirror as the primary concentrator. As the second concentrator, a tailored non-imaging collector is used to concentrate the solar radiations at the Nd: YAG rod. The achieved power from the solar-powered laser is 57 W. Further, in 1999, two solar lasers, including a Q switched Nd: YAG laser with type II potassium titanyl phosphate (KTP) crystal for intracavity frequency doubling and a red alexandrite laser are demonstrated [77]. Considering the passive Q-switching, Lando et al. revealed that it is an excellent choice for space applications with low cost, reliability and simplicity of operation. Thus to surpass the lasing threshold, the highly concentrated solar radiation is collected by a 3-stage concentrator. The combination of concentrators consists of 12 Fresnel parabolic heliostats, three-dimensional (3D) CPC and two-dimensional (2D) CPC. For Nd: YAG second harmonic generation, output powers of 4.1 W and 8.7 W are obtained via passive and active Q-switching, respectively. The output power of up to 12 W is achieved from the alexandrite laser, which is maximum than the Q switched Nd: YAG solar laser. In the year 2003, Lando et al. undertook another expansion to the solar-powered lasers in the context of collection efficiency and beam quality [95]. The Nd: YAG solar laser with a 6.75 m^2 segmented primary mirror and a secondary 3D CPC conjugated with a 2D CPC is utilized to increase the collection efficiency up to 6.7 W/m^2. The authors also evaluated the laser beam quality with brightness and reported the brightness figure of merit of 0.032 W. This is recorded as the highest collection efficiency of solar-powered solid-state Nd: YAG lasers until the year 2007.

After the continuous use of parabolic mirrors, rapid progress has been made in solar-powered solid-state Nd: YAG lasers from the adoption of the Fresnel lens [21]. In the year 2007, first time, Yabe et al. proposed an end-pumped solar laser with Cr: Nd: YAG gain medium and a Fresnel lens of size 1.3 m^2 for renewable recovery of magnesium (Mg) from magnesium oxide (MgO). The utilization of the Cr^{3+} ion enabled efficient absorption of solar radiations in the visible spectrum. Thus, the co-doping of chromium ions in Nd: YAG crystal improves the laser efficiency. The authors revealed an output power of 24.4 W with 11-14% of slope efficiency and 18.7 W/m^2 of collection efficiency. In 2009, Ohkubo et al. proposed a side-pumped Cr: Nd: YAG solar laser with a

$4m^2$ Fresnel lens with high output power and collection efficiency [96]. The output power of the proposed system is 80 W with a conversion efficiency of 4.3%. The authors concluded that collection efficiency of new solar-powered laser is 20 W/m^2, which is 2.99 times larger than previous results with the mirror-type concentrator [95].

In 2011, Liang and Almeida show a significant improvement in the performance of solar lasers by employing a Fresnel lens and dielectric totally internally reflecting concentrator (DTIRC) [25]. The Fresnel lens of 0.9 m collects the incoming solar radiation. The DTIRC is added to couple the focused solar radiations from the focal zone of Fresnel lens to a Nd: YAG rod (4 mm diameter and 25 mm length) within a conical pump cavity. The proposed system produces the 12.3 W output power corresponding to 19.3 W/m^2 collection efficiency, which is 2.9 times larger than the previous record of 6.7 W/m^2 with a large diameter Nd: YAG rod and a mirror type concentrator [95]. The collection efficiency of the proposed solar laser even slightly higher than the collection efficiency of 18.7 W/m^2 by utilizing a large Cr: Nd: YAG ceramic rod and a Fresnel lens [21].

By the 2010s, the scientific community began their research on the second concentrator and pumping cavity by keeping the Fresnel lens as the primary concentrator [96]. In the year 2012, Dinh and the group proposed a 120 W solar-powered solid-state laser with a simple and efficient pumping method [45]. The laser system comprises of a 2×2 m Fresnel lens, liquid light guide lens, and hybrid pumping configuration. The achieved collection efficiency from the solar laser is 30 W/m^2, which is 1.5 times higher than the previous record [96]. Dinh et al. also compared the results from Cr: Nd: YAG ceramics and Nd: YAG laser rod and declared that the obtained results are better with Nd: YAG crystal. Despite the similar saturation gains, the scattering coefficient of Cr: Nd: YAG ceramics is double that of Nd: YAG crystal. In 2012, Liang and Almeida also presented a new idea of thin-disk laser technology by the combination of mirrors and Fresnel lenses. The presented system perfectly reduced the thermal management problem [97].

Given the different modes of solar-powered Nd: YAG lasers, the first TEM$_{00}$ mode solar-pumped laser was developed for a smooth intensity profile in 2013 [98]. The Fresnel lens of 1 m diameter is used to collect the incoming solar radiation. Further, a large aspheric lens and 2D CPC are combined to compress the concentrated sunlight at the thin laser rod within the V-shaped pumping cavity. The output power from the developed continuous-wave (CW) TEM$_{00}$ solar laser is 2.3 W, corresponding to 1.9-watt beam brightness figure of merit and 2.93 W/m^2 of collection efficiency [98].

After the employment of the polished and unpolished Nd: YAG rod, for the first time, a solar-powered laser with Nd: YAG grooved rod was developed in the year 2014. The collection efficiency and beam quality are improved relatively more with Nd: YAG grooved rod than the polished and unpolished rods. Xu et al. analysed the performance of different rods. They revealed that the output power is 50% higher in grooved rod than in unpolished rod because it offers better heat dissipation that decreases the thermal lens effect [99]. Further, a grooved Nd: YAG rod is also tested in two different cavities, ceramic conical cavity and copper conical cavity. The output power achieved from the ceramic conical cavity is 20 W, corresponding to optical–optical efficiency of 4.85%. However, the output power with the copper conical cavity is 27 W, corresponding to an optical–optical efficiency of 6.44%, which is higher than ceramic conical cavity [99].

Taking a radically different approach to the luminescent solar concentrator (LSC), Reusswig et al. presented an architecture for solar-powered lasers. Instead of using a parabolic and Fresnel concentrator, a 750 μm thick Nd^{3+}doped YAG planar waveguide sensitized by a luminescent CdSe/CdZnS (core/shell) colloidal nanocrystal is utilized for the collection of solar radiations [100]. This system essentially creates a peak cascade energy transfer of 14% and an equivalent quasi-CW solar lasing threshold of approximately 230 suns.

In 2016, from simulation analysis, Payziyev et al. studied the possibility of improving the laser efficiency of Nd: YAG solar lasers with the employ of Cr: LiCAF as a solar spectrum frequency downshifting element [101]. Subsequently, numerical experiments have been conducted to compare side and end pumping methods. The result declared that utilizing Cr: LiCAF frequency down shifter significantly enhances the pumping efficiency of Nd: YAG active medium in both pumping methods.

Considering the dependency of solar concentrators on precise solar tracking, Masuda and the group demonstrated a solar-powered laser that does not depend on any conventional concentrators (parabolic mirror, Fresnel lens) or solar tracking system. The new type of solar-powered laser has potential applications in the long-term renewable energy storage or decentralized power supplies for electric vehicles and Internet of Things devices [102]. In 2017, the proposed solar laser used an Nd^{3+} doped silica fiber with transverse excitation geometry. A 40 m long Nd^{3+} doped silica fiber is packed in a ring chamber filled with a sensitizer solution. However, the sunlight is concentrated through the toroidal lens, and the system still depends on the lens and solar tracker device. With this system, the produced lasing threshold is 15 times the concentrated solar radiation and two orders of magnitude smaller than that of conventional solar lasers.

In 2018, the researcher started work on a different approach to the solar-powered laser by co-doping cerium (Ce^{3+}) ions in Nd: YAG crystal to improve the laser efficiency. The cerium ions have strong absorption bands in visible spectral regions that overlap with the solar emission spectrum. Payziyev and the group demonstrated a simulated model of Ce: Nd: YAG solar-powered laser with increased slope efficiency and output power [50]. Based on the experimental investigation, the first Ce: Nd: YAG laser system is proposed by Vistas et al. [61]. The authors presented a solar-powered laser with Ce: Nd: YAG rod (5 mm diameter, 30 mm length) in an end-side-pumped configuration and compared the performance with Nd: YAG rod (5 mm diameter, 30 mm length). The incident solar radiations are initially collected via a parabolic mirror (1.23 m^2), and a fused silica liquid light guide lens is used to couple the concentrated solar radiations into the laser medium. Based on the comparison, the output power of the Ce: Nd: YAG solar-powered laser is 6 W, corresponding to the collection efficiency of 4.9 W/m^2, while the Nd: YAG laser system produced power of 10 W, corresponding to the collection efficiency of 8.1 W/m^2 [61]. The authors concluded that the lower output of Ce: Nd: YAG solar-powered laser is due to the Ce co-dopant, which may account for an immense scattering loss within the crystal [40,103]. The end-side-pumped configuration also increased the thermal load of the laser rod.

In 2020, Masuda et al. demonstrated a fully planar solar laser that utilized a luminescent solar concentrator (LSC) rather than a lens or solar tracking system. The proposed system consists of an Nd^{3+} doped silica fiber and a dichroic mirror to transmit incoming solar radiations and trap the fluorescence emitted by the sensitizer [23,104]. The experiment results declared that the conversion efficiency from solar radiation to laser output reached 8%. Previously, the working of the solar-powered laser was based on radiative energy transfer from a luminescent dye solution. In 2021, Dottermusch et al. proposed the design of solid-state luminescent solar concentrators for solar pumping of fiber lasers. The prime advantage of solid LSC design is introducing TIR (total internal reflection) to the system. The liquid-based solar lasers used the reflective cavity only, but the solid-based LSC utilized both the reflective cavity and TIR [105].

After the successful invention of the Ce: Nd: YAG solar-powered laser, Vistas et al. proposed a system with a side-pumped configuration instead of an end-side-pumped configuration to avoid the inhomogeneous heating of laser rod [62]. The NOVA heliostat-parabolic mirror collects and concentrates the incident solar radiations [62]. The solar-powered laser head consists of a fused silica semispherical lens and a two-dimensional (2D) trapezoidal-shaped pumping cavity. The obtained power from the proposed system is 16.5 W with 23.6 W/m^2 of collection efficiency, 2.8% of solar-to-laser power conversion efficiency, and 4.4 % slope efficiency. Based on the comparison analysis, the Ce:

Nd: YAG side-pumped solar laser has 1.39 and 1.15 times more collection efficiency and solar-to-laser power conversion efficiency, respectively, than the previous record by Nd: YAG side-pumped solar laser [39]. The authors also concluded that the collection efficiency, slope efficiency, and solar-to-laser power conversion efficiency of Ce: Nd: YAG side-pumped configuration are 4.82, 4.00, and 4.67 times higher, respectively, than the Ce: Nd: YAG end-side-pumped solar laser [61].

Recently, the research community has started working on the simultaneous emission of several laser beams rather than a single beam [41,106–111] . This concept distributes the concentrated solar radiation among multiple rods that reduce the thermal stress effects. Tibúrcio et al. presented the novel idea of a dual-rod solar-pumped laser based on the simulation analysis [106]. The proposed side-pumped dual-rod Nd: YAG solar laser head consists of the semicylindrical fused silica lens and the CPC-semicylindrical pump cavity. Each Nd: YAG laser rod is pumped by half of the solar concentrator area. Based on comparative analysis with the previous experimental study [54,42,112], significant enhancements in collection efficiency (11 W/m^2), output power (17.2 W), incoming solar power to TEM_{00} mode laser power conversion efficiency (1.31%) and brightness conversion efficiency (1.10 %) is achieved. At the same time, due to the lower pumping intensity on each rod, the heat load, temperature, and stress intensity are lower in the dual-rod scheme than in the single-rod system [106].

After implementing the multi-rod concept, Liang et al. proposed the first simultaneous emission of three CW solar-powered laser beams by three end-side-pumped Nd: YAG rods within a single conical pump cavity [108]. The achieved output power from the multimode solar laser is 18.3 W with a laser slope efficiency of 5.1%. The obtained 0.036 W laser beam brightness figure of merit from the presented solar laser is 9 times more [108] than the most efficient solar-powered laser with 32.5 W/m^2 of collection efficiency [53]. The authors also declared that by increasing the resonant cavity length from the AR1064nm laser rod end face, different output power and beam profiles are obtained for the three rods [108]. In 2021, Liang and the group proposed a new solar-powered laser with a seven-rod pumping approach for the efficient production of the TEM_{00} mode beam [111]. The proposed system consists of a 4.0 m^2 Fresnel lens as the primary solar concentrator and a fused silica aspheric secondary concentrator to pump seven (2.5 mm diameter, 15 mm length) Nd: YAG rods within a conical pump cavity. The authors used the seven individual plane-concave large-mode resonators to enable a good overlap between solar pump mode and TEM_{00} laser oscillating mode [111]. The output power of the TEM_{00} mode solar-powered laser is 54.65 W, which is numerically calculated by optimizing the radius parameter of the Fresnel lens, the diameter of the laser rod, and the radius of curvature of the laser resonator output mirror. The achieved collection efficiency and solar power-to-TEM_{00} mode laser power conversion efficiency is 13.66 W/m^2 and 1.44%, respectively. Compared to the experimental records of the TEM_{00} mode solar laser, the collection efficiency and solar power-to-TEM_{00} mode laser power conversion efficiency are increased to 4.66 times and 4.38 times, respectively [111].

In recent, Liang and the group demonstrated a most efficient solar-powered laser for the simultaneous emissions of three beams via three Ce: Nd: YAG rods within a single pump cavity [63]. The parabolic mirror (0.4 m^2) and fused silica aspheric lens are utilized as the primary and secondary concentrators, respectively, to focus the concentrated solar radiation into three laser rods (2.5 mm diameter, 25 mm length). With the 356 W of incoming solar power, the proposed system produced 16.5 W of CW multimode solar laser power, corresponding to a 4.64 % solar-to-laser conversion efficiency, 41.25 W/m^2 collection efficiency, and 7.64 % slope efficiency [63]. Based on the comparative analysis with the three Nd: YAG laser rods (3.0 mm diameter, 25 mm length) [108], the Ce: Nd: YAG rods provide the 2.13, 2.25 and 1.50 times enhancements in solar-to-laser conversion efficiency, collection efficiency, and slope efficiency, respectively [63].

The laser beam merging approach can be an alternative to produce the Gaussian laser beams of high power with high beam brightness [113]. A novel zigzag multi-rod laser beam merging technique for the solar-powered laser is proposed by Costa et al. to provide a better overlap between the pump and the fundamental mode volumes [113]. The solar light is collected and concentrated via megawatt solar furnaces (MWSF). Additionally, the presented solar-powered laser consists of a solar flux homogenizer with hexagonal shaped faces and multiple arrays of core-doped Nd-YAG rods placed after a fused silica window at the homogenizer's output face [113]. The presence of the homogenizer delivered approximately the same amount of solar power to pump each rod, and also the substantial reduction of the thermal lensing effects on each rod. Based on the numerical calculation, the authors attained 1.06 W of average power from each rod and 1.8 kW power from all 1657 rods. The incredible work of a TEM_{00} mode solar laser based on pumping techniques, laser beam profiles, beam merging methods, and multi-beam production has opened a new door for solar-powered laser advancement [114].

Recently, Tibúrcio and the group proposed a study based on the tracking error compensation capacity measurement of a dual-rod side-pumping solar laser [115]. The authors presented the first experimental results of tracking the error compensation capacity of a solar laser, with a primarily enhanced tracking error tolerance obtained by pumping two laser rods simultaneously. A parabolic mirror is used as the primary concentrator, and a large aspherical fused silica lens is employed as a secondary concentrator to efficiently focus the concentrated solar radiation onto the two laser rods. A significant improvement in tracking error compensation capacity is experimentally achieved, leading to an increment in tracking error width at 10% laser power loss ($TEW_{10\%}$) of 14.0 and 6.0 times in its vertical and horizontal setups, respectively [115]. Compared to the previous dual-rod scheme using a semi-cylindrical lens and a CPC pump cavity, the $TEW_{10\%}$ is enhanced by 3.9 and 1.7 times, respectively, with the vertical and the horizontal setups [115].

The 55 years historical point of view of solar-powered solid-state lasers involving solar concentrators, laser medium, pumping schemes, output power, collection efficiency, and solar-to-laser conversion efficiency are summarized below in Table 2.

4. Review of solar concentrator

The direct utilization of solar radiation has motivated acute research for practical solar power systems to accomplish human energy needs [128]. However, most solar energy applications demand high temperatures; hence, it becomes essential to focus solar radiation efficiently [129]. The power density of radiations obtain from the sun on the earth's surface is low, which is insufficient for irradiating the active medium of solar-pumped lasers. Thus, concentrating optics is needed with the assistance of mirrors or lenses to increase the power density of natural sunlight. The solar concentrators can be classified based on their working principles, image formation, and tracking mechanism, as illustrated in Fig. 11 [130–132].

Based on the working principle of reflection, refraction, hybrid, and luminescence, solar concentrators are categorized into four groups as described below [131,132]:

I Reflection: The solar collector is oriented to reflect incoming sunlight toward the laser medium. The working of these collectors is based on the principle of reflection. Under this category, numerous reflecting concentrators are present, including the parabolic dish, parabolic trough, hyperboloid concentrator, compound parabolic concentrator etc.

II Refraction: In this case, when the incoming solar radiations hit the collectors, the sunrays will be refracted to the laser medium. An example of such refracting collectors is the Fresnel lens, which works on the principle of refraction.

III Hybrid: This type of collector, concentrates the solar radiations towards the focal point by employing the principle of reflection

Table 2
State-of-the-Art of solar-pumped solid-state lasers.

Year	Research group	Primary concentrator	Secondary concentrator	Laser Medium	Pumping method	Output power (W)	Collection efficiency (W/m²)	Solar-to-laser conversion efficiency (%)	Results
1966 [37]	Young	Paraboloidal mirror	Hyperbolic-cylindric, hemicircular cylindric mirror	Nd: YAG rod	Side	1	-	0.36	Experimental
1984 [38]	Arashi et al.	Paraboloidal mirror	Mounting directly at the focus	Nd: YAG rod	Quasi-side	18	-	-	Experimental
1988 [66]	Weksler et al.	600 spherical mirrors	2D CPC	Nd: YAG rod	Side	60	-	-	Experimental
1996 [94]	Jenkins et al.	25 hexagonal segments, parabolic mirror	Tailored non-imaging concentrator	Nd: YAG rod	Side	57	4.7	0.495	Experimental
1999 [47]	Lando et al.	12 Fresnel parabolic heliostats	3D CPC, 2D CPC	AR coated Nd: YAG rod	-	4.1, 8.7	-	0.71	Experimental
2003 [95]	Lando et al.	Segmented parabolic mirror	3D CPC, 2D CPC	Nd: YAG rod	Side	46	6.7	-	Experimental
2007 [22]	Yabe et al.	Fresnel lens	Cylindrical cavity	Cr: Nd: YAG rod	End	24.4	18.7	2.9	Experimental
2009 [96]	Ohkubo et al.	Fresnel lens	Pumping cavity as secondary concentrator	Cr: Nd: YAG rod	Side	80	20	4.3	Experimental
2011 [25]	Liang et al.	Fresnel lens	DTIRC	Nd: YAG rod	End-side	12.3	19.3	2.76	Experimental
2012 [45]	Dinh et al.	Fresnel lens	Liquid light guide lens	Nd: YAG rod	Hybrid (End-side)	120	30	-	Experimental
2012 [116]	Almeida et al.	Parabolic mirror	Fused silica light guide, 2D CPC	Nd: YAG rod	Side	27.7	9.6	1.38	Experimental
2013 [52]	Liang et al.	Parabolic mirror	Fused silica light guide	Cr: Nd: YAG rod	Side	33.6	11.7	1.93	Experimental
2013 [46]	Liang et al.	Fresnel lens	DTIRC	Nd: YAG rod Cr: Nd: YAG ceramic rod	End	12.3 13.5	19.3 21.2	2.76 3.03	Experimental
2013 [117]	Almeida et al.	Heliostat–parabolic mirror	Fused silica light guide with 3D CPC output end	Nd: YAG rod	End	40	13.9	2.3	Experimental
2014 [99]	Xu et al.	Fresnel lens	Ceramic conical cavity secondary concentrator	Grooved and unpolished Nd: YAG rod	End-side	20.3 27	19.7, 26.14	4.8, 6.44	Experimental
2014 [118]	Almeida et al.	Four Fresnel lens	Four-fused silica semi-cylindrical lens	Nd: YAG rod	Side	83	20.8	2.87	Numerical
2014 [119]	Liang et al.	Four Fresnel lens	Fused silica aspheric lens	Nd: YAG rod	Side	59.1	14.8	2.11	Numerical
2015 [120]	Almeida et al.	Parabolic mirror	Fused silica conical lens	Nd: YAG rod	End-side	56	21.1	3.67	Experimental
2015 [42]	Vistas et al.	Heliostat-parabolic mirror	Fused silica semi-cylindrical lens	Grooved Nd: YAG rod	Side	4	3.6	0.54	Experimental
2015 [121]	Almeida et al.	Parabolic mirror	2D trapezoidal light guide	Nd: YAG rod	Side	5.5	2.84	0.55	Experimental
2015 [122]	Liang et al.	Parabolic mirror	Fused silica light guide, 2D CPC	Nd: YAG rod	Side	4.4	1.91	0.39	Experimental
2016 [123]	Liang et al.	Parabolic mirror	Fused silica aspheric lens	Nd: YAG rod	End-side	29.3	25	3.75	Experimental
2016 [124]	Oliveira et al.	Parabolic mirror	Conical cavity as secondary concentrator	Cr: Nd: YAG rod	End-side	19.2	12	1.81	Experimental
2017 [125]	Bouadjemine et al.	Parabolic mirror	2D CPC	Nd: YAG rod	Side	2.3	1.96	-	Experimental
2017 [126]	Mehellou et al.	Parabolic mirror	Fused silica twisted light guide, 2D CPC	Nd: YAG rod	Side	2.7	2.3	0.44	Experimental

Table 2 (*continued*)

Year	Research group	Primary concentrator	Secondary concentrator	Laser Medium	Pumping method	Output power (W)	Collection efficiency (W/m^2)	Solar-to-laser conversion efficiency (%)	Results
2017 [54]	Liang et al.	Parabolic mirror	Fused silica aspheric lens	Nd: YAG rod	End-side	37.2, 9.3	31.5, 7.9	5.31, 1.32	Experimental
2018 [53]	Liang et al.	heliostat-parabolic mirror	Fused silica light guide lens	Cr: Nd: YAG ceramic rod	End-side	32.5	32.5	3.74*	Experimental
2018 [127]	Guan et al.	Fresnel lens	Conical cavity as secondary concentrator	Grooved bonding Nd: YAG rod	End-side	33.1	32.1	3.31*	Experimental
2019 [91]	Vistas et al.	Parabolic mirror	Fused silica liquid light guide	Nd: YAG rod	End-side	4.5	4.5	0.54*	Experimental
2019 [39]	Liang et al.	Parabolic mirror	Fused silica aspheric lens	Nd: YAG rod	Side	15.3. 2.8, 2.9	17, 3.1, 3.2	2.43*, 0.40*, 0.46*	Experimental
2019 [106]	Tibúrcio et al.	Parabolic mirror	Semicylindrical fused silica lens	Nd: YAG rod (two-rod)	Side	17.2	11	1.31*	Numerical
2020 [110]	Almeida et al.	Parabolic mirror	Fused silica CPC	Nd: YAG rod (seven-rod)	End-side	23.4	13.3	1.40*	Numerical
2020 [61]	Vistas et al.	Parabolic mirror	Fused silica light guide lens	Ce: Nd: YAG rod	End-side	6	4.9	1.05	Experimental
2021 [62]	Vistas et al.	Parabolic mirror	Fused silica semispherical lens	Ce: Nd: YAG rod	Side	16.5	23.6	2.8*	Experimental
2021 [113]	Costa et al.	Parabolic mirror	Hexagonal hollow homogenizer	Nd: YAG rod (1657)	End-side	1800, 200	-	-	Numerical
2021 [111]	Liang et al.	Fresnel lens	Fused silica aspheric lens	Nd: YAG rod (seven-rod)	End-side	54.65	13.66	1.44*	Numerical
2021 [93]	Catela et al.	Fresnel lens	Fused silica aspheric lens	Nd: YAG rod	Side	37.5, 39	9.4, 9.8	0.99*, 1.03*	Numerical
2022 [60]	Garcia et al.	Parabolic mirror	Fused silica aspheric lens	Ce: Nd: YAG rod	End-side	11.2	38.22	4.50*	Experimental
2022 [59]	Vistas et al.	Parabolic mirror	Fused silica aspherical lens, rectangular fused silica light guide	Ce: Nd: YAG rod	Side	19.6, 17.4	18, 16	1.74*, 1.54*	Experimental
2022 [63]	Liang et al.	Parabolic mirror	Fused silica aspheric lens	Ce: Nd: YAG rod (three-rod)	End-side	16.5	41.25	4.64*	Experimental

* Solar-to-laser conversion efficiency based on the total incoming solar power
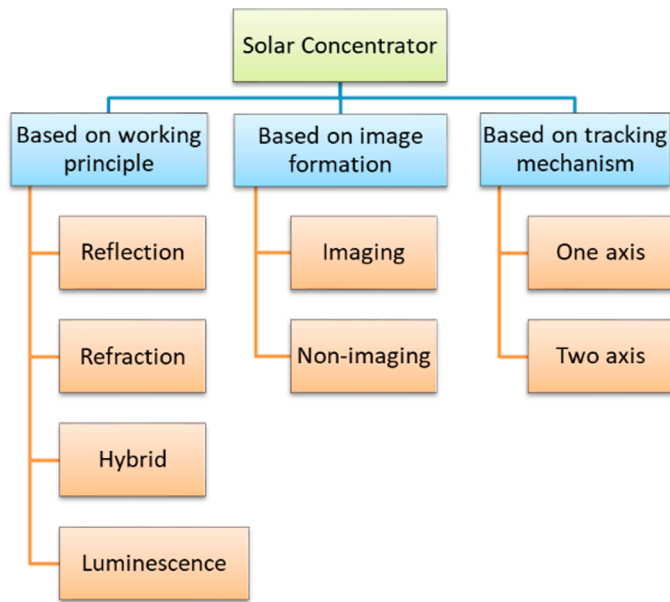
Fig. 11. Classification of solar concentrator.

and refraction. Dielectric totally internally reflecting concentrator and flat high concentration device (FHCD) come under the consideration of hybrid concentrator.

IV Luminescence: In the case of luminescent collectors, the photon will experience total internal reflection and guiding light towards the laser medium. A Quantum dot concentrator is an example of a luminescent solar collector.

The solar concentrators can be divided on the basis of image formation, whether the concentrator is imaging or nonimaging [131–133]. Fig. 12 illustrates the imaging and nonimaging solar concentrator. Imaging concentrators focus the solar radiations onto a focal point, thus creating an image of the light source. Nevertheless, the image is dispersed when the incident sunrays are not parallel to the axis of the concentrator. Paraboloid is the most common example of an imaging concentrator with the working principle of reflection [133]. Further, the imaging concentrator is divided into point focusing and line focusing.

In 1965, nonimaging optics was discovered to collect energy rather than form an accurate sun image [133]. The nonimaging concentrator considers only the boundary of the transmitted light beam rather than
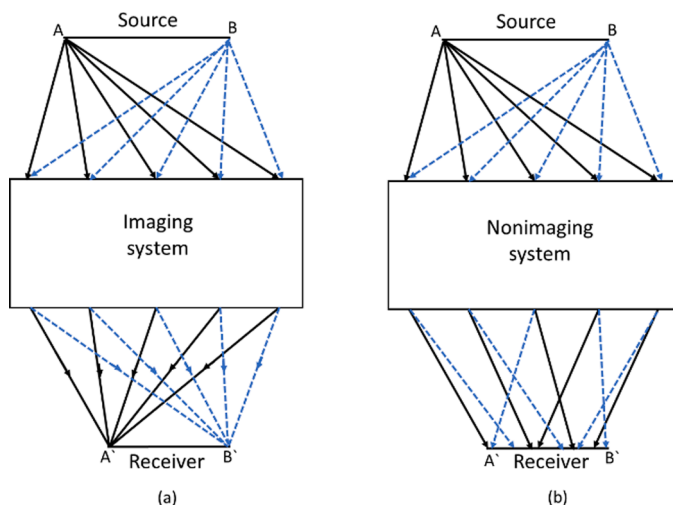
the interior order of the transmitted light rays. The most common example of a nonimaging concentrator is CPC [134].

Based on the tracking mechanism, the solar concentrators can be either one-axis or two-axis [132]. Solar concentrators, if rotated along one axis to receive the maximum beam radiation across the aperture, are known as one-axis concentrators, such as CPC, linear Fresnel lens reflector/refractor etc. [132]. In two-axis tracking concentrator, maximum energy collection with a high concentration ratio is achieved due to the freedom of movement of the solar concentrator. The two axes tracker allows the concentrator to face the sun's rays throughout the day with different seasons. The solar-pumped lasers require two-axis sun-tracking systems for the efficient capture of the solar radiation during the day and along the year. Additionally, the solar concentrators can be categorized as 2D concentrators and 3D concentrators [133]. This section is divided into three subsections. The first part explains the optical parameters for solar concentrators, and the further subsections describe the primary, secondary, and tertiary concentrators.

4.1. Design parameters of solar concentrator

The fundamental problem of the concentrator is how the sun rays with a specified angular divergence distributed over an entrance aperture can direct efficiently onto the smallest possible exit aperture with the highest possible concentration [92]. Several parameters are used for characterizing the concentrating system. These parameters are classified as aperture area, absorber area, acceptance angle, concentration ratio, intercept factor, and optical efficiency [135–137].

I Aperture area (A_a): The area through which incident solar radiations are accepted. In a linear concentrator, the aperture area is determined by the width. In contrast, a surface of revolution is defined by the diameter of the opening [135].

II Absorber area (A_{abs}): The total area on which the concentrated radiations are received and from which useful radiations are delivered to the laser medium [136].

III Acceptance angle ($2\theta_a$ or $2\theta_{max}$): This angle defines the extent to which the incident ray may deviate from the normal to the aperture plane and still reach the receiver without moving the concentrator. A concentrator with a large acceptance angle requires only seasonal adjustment, while a concentrator with a small acceptance angle needs to track the sun continuously [134].

IV Concentration ratio (C): The most critical factor of a solar concentrator is the concentration ratio, which is defined as the ratio of the collecting aperture area (A_a) and absorber area (A_{abs}), as shown in Eq. 20 [134]. The concentrating systems can be classified based on their concentration ratio [133]. A concentration ratio of less than 10 × are low concentration system, while for concentration ratio between 10 × and 100 × is considered a medium concentrator, and a concentration of greater than 100 × is called a highly concentrated system.

$$C = \frac{A_a}{A_{abs}} \tag{20}$$

V Intercept factor (γ): it is defined as the ratio of energy intercepted by the absorber of a chosen size to the total energy reflected/refracted by the focusing device [135].

VI Optical efficiency (η_o): it is defined as the ratio of the energy absorbed by the absorber to the energy incident on the concentrator's aperture. The optical efficiency is affected by the shape of a concentrator, incidence angle of solar radiation, reflection or transmission losses, and tracking accuracy [135].

Fig. 12. Solar concentrator (a) Imaging, (b) Nonimaging types.

4.2. Primary concentrator

For solar-pumped solid-state lasers, concentrators are subdivided into primary, secondary and tertiary parts. Most solar-powered solid-state laser studies have adopted the parabolic mirror and Fresnel lens as the primary concentrator. As briefly discussed in section 3.5, from 1966 to 2006, a parabolic (paraboloid d) mirror was employed to collect solar radiations. However, the heliostat-parabolic mirror system is complicated and has shadow zones between the laser head and the sun's beams. Since 2007, the Fresnel lens has been used successively as a primary concentrator, which is responsible for significantly improving laser collection efficiency. However, utilizing the Fresnel lens for direct solar tracking of laser systems, where the solar laser head usually moves together with the entire solar tracking structure, has several practical drawbacks [25,46]. Therefore, an optical fiber is needed to transfer laser radiation to a fixed target, which reduces the efficiency of the solar laser owing to coupling and transmission losses. Hence, the research community also used a ring array concentrator to focus the solar radiations efficiently at the laser head. This subsection is further classified into the parabolic concentrator, Fresnel concentrator, and ring array concentrator.

4.2.1. Parabolic mirror

The parabolic concentrator is mainly utilized as a reflecting concentrator, focusing parallel solar radiations onto a focal point. The accomplished concentration through the parabolic concentrator is known as 2D concentration and 3D concentration [134]. When the solar radiation is focused onto a line, it is known as 2D concentrator and obtained through a parabolic trough. Similarly, 3D concentration is attained by focusing the rays onto a point via a parabolic dish. The equation that defines a parabola with the vertex at (x, y) = (0, 0) is given by Eq. 21

$$y = ax^2 \tag{21}$$

The aperture (a) and focal length (f) of the parabola are correlated, as shown in Eq. 22

$$f = \frac{1}{4a} \tag{22}$$

The functional relation that defines the geometry of a parabola with its axis aligned with the y-axis is represented by Eq. 23

$$y = \frac{x^2}{4f} \tag{23}$$

A paraboloid (a parabolic surface of revolution) with its axis coinciding with the z-axis is shown in Eq. 24 [137,138]

$$z = \frac{r^2}{4f} = \frac{x^2 + y^2}{4f} \tag{24}$$

The parabolic mirror focuses on a single point only when the incoming radiations are parallel. However, sunrays have a range of incident angles because of the physical extent of the sun. Hence, the optical concentration obtained at the parabola's focus is reduced [137,138]. Therefore, it is necessary to understand the rim angle for optimizing the solar flux collection. The rim angle ($\emptyset_R$) is described as the angle formed by the axis and a line from the focus to the physical edge (rim edge) of the parabolic mirror. The rim angle of the parabolic concentrator is calculated from Eq. 25

$$tan\emptyset_R = \frac{W/2}{f - Z_R} = \frac{4fW/2}{4f^2 - (W/2)^2} \tag{25}$$

where W is the width, and Z_R is the depth of the parabola at the rim. Rim angle is also responsible for characterizing the flatness of the shape of a finite parabolic mirror. The parabolic concentrator becomes more curved when the rim angle increases, but the focal length reduces. Thus,

the cross-section geometry of a parabolic concentrator can be described from focal length and rim angle.

The absorber for concentrating solar radiation from the parabolic mirror can be a flat or circular cross-section [137,138]. As illustrated in Fig. 13, each point on a parabolic mirror will reflect a cone of rays that matches the angular distribution of the sun (acceptance half-angle, θ_S). The concentrated solar radiations will occurrence on the flat target placed at the parabolic mirror's focal plane, and the rays from the rim will form the broadest spot. The distance of the x (reflection point) from the vertical axis is calculated from Eq. 26. Similarly, the width of the focus spot from the point x is represented by Eq. 27

$$x = rsin\emptyset_R \tag{26}$$

$$d = \frac{2rsin\theta_S}{cos\emptyset_R} \tag{27}$$

If r is approximately equal to f, and the $\emptyset_R$ is small then the true image of the sun at the focal plane of the mirror with diameter is calculated by Eq. 28

$$d = \frac{2fsin\theta_S}{cos0} = 2fsin\theta_S \tag{28}$$

$$C_{g,trough} = 68.5$$

Nevertheless, in the case of a trough and dish with a flat receiver and a rim angle of 90°, the formed image will be infinitely long. The geometric concentration ratio for a parabolic trough with a flat receiver is expressed by Eq. 29

$$C_g = \frac{sin2\emptyset_R}{2sin\theta_S} \tag{29}$$

By putting the $\emptyset_R = 45°$ and $\theta_S = 4.465$ mrad, the maximum concentration ratio of a trough and dish is given below [137,138]

$$C_{g,trough} = 108, \text{ and } C_{g,dish} = 11,600$$

When a receiver has a circular cross-section, then the concentration ratio of a trough is calculated by Eq. 30

$$C_{g, trough} = \frac{sin\emptyset}{\pi sin\theta_S} \tag{30}$$

where $\emptyset$ is the rim angle and by putting the $\emptyset = 90°$, the maximum concentration ratio of a trough and dish is calculated [137].

For a parabolic dish concentrator with a spherical receiver, the maximum concentration ratio is calculated by Eq. 31
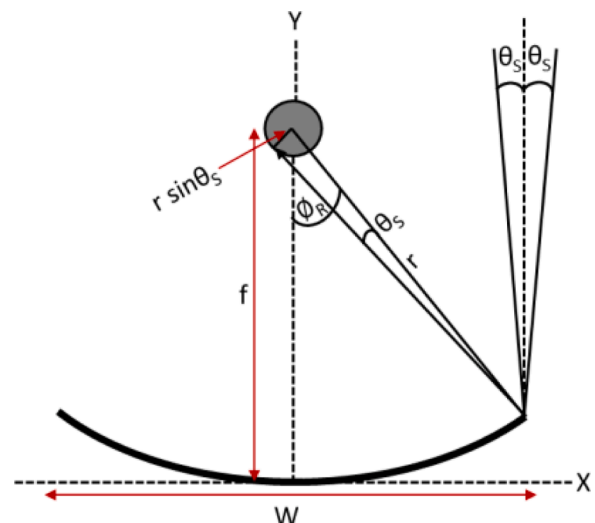

Fig. 13. Parabolic mirror with circular cross-section receiver [137,138].

$$C_{g,\ dish} = \frac{sin^2\varnothing}{4sin^2\theta_S} \tag{31}$$

As a primary concentrator of solar-powered solid-state laser, a parabolic mirror is an efficient optical element to collect and concentrate the solar radiations at a focused spot. In the year 2017, Liang et al. remarked on the tremendous performance of a Nd: YAG laser with the parabolic mirror [54]. The proposed system determined the 37.2 W continuous-wave multimode solar laser power, corresponding to 31.5 W/m² multimode laser collection efficiency and 8.9% slope efficiency at the focus [54]. In 2022, Garcia et al. recorded the highest collection efficiency of the Ce: Nd: YAG solar laser [60]. The parabolic mirror (0.293 m²) with fused silica aspheric lens is utilized to focus the solar radiations at the laser rod. Moreover, the highest solar laser collection efficiency of 38.22 W/m² and slope efficiency of 6.8% is obtained, which are 1.18 and 1.02 times, respectively, higher than the previous records [53]. Recently, Liang and the group employed the parabolic mirror (0.4 m²) as the primary concentrator for simultaneous solar laser emissions [63]. A fused silica aspheric lens is utilized to couple the concentrated solar radiation from the focal zone of parabolic mirror into three Ce: Nd: YAG laser rods (2.5 mm diameter, 25 mm length) within a single conical pump cavity. The proposed solar-powered laser generates 16.5 W continuous-wave total multimode solar laser power, corresponding to 4.64% solar-to-laser conversion efficiency, 41.25 W/m² collection efficiency, and 7.64% slope efficiency [63].

4.2.2. Fresnel lens

Fresnel lens is the most generic concentrator for solar laser. Most Fresnel lenses have been imaging devices employed as primary concentrators for collecting solar radiation. Now nonimaging Fresnel lenses are begun to utilize for solar-powered lasers. Compared to conventional concentrators, the Fresnel lens has various advantages, including the small volume, reduction in lens thickness, lightweight, mass production with low cost, and high energy density efficiency [139]. In 1822, the Fresnel lens was discovered by Augustin Jean Fresnel as the collimator for the lighthouse. The first material used to fabricate the Fresnel lens was glass. After that, in the 1950s, polymethylmethacrylate (PMMA) material was used to manufacture the lens [140]. The first employ of the Fresnel lens for collecting the solar radiations has occurred when the suitable PMMA material is utilized [130] since the transitivity of the PMMA lens matches the solar spectrum. A Fresnel lens has a chain of prisms, and its working is based on the principle of refraction. Fig. 14 shows that the imaging Fresnel lens works as a concentrator. Generally, the design of the imaging lens is realized on paraxial rays, and there is no acceptance of half-angle [131].

Three Eq. 32,33, and 34 are expressed to represent the Fresnel lens. The prism angle (α) is the main factor for the simulation of the lens. The incident ray on the lens follows Snell's law as shown in Eq. 32, where α is

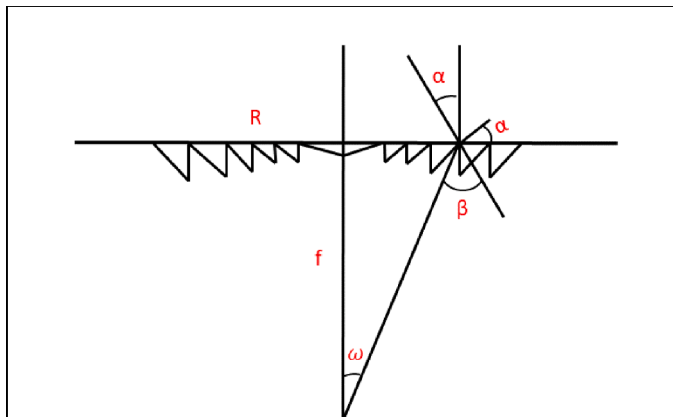**Fig. 14.** Imaging Fresnel lens as a solar concentrator [131].

the angle between the lens facet and the incident ray, and β is an angle between the normal direction of the lens's facet and the refraction ray, and n is the refractive index.

$$n\sin\alpha = \sin\beta \tag{32}$$

$$\tan\omega = \frac{R}{f} \tag{33}$$

where f is the focal length of lens, R is the distance between incident ray and centre axis of the lens, and ω is the angle between the refracted ray and the normal of the receiver. Eq. 34 shows the angle, β

$$\beta = \alpha + \omega \tag{34}$$

By substituting the β in Eq. 32, the expression for tanα is shown in Eq. 36

$$n\sin\alpha = \sin\alpha\cos\omega + \cos\alpha\sin\omega \tag{35}$$

$$\tan\alpha = \frac{\sin\omega}{n - \cos\omega} \tag{36}$$

tanα can also be written as

$$\tan\alpha = \frac{R}{f}\frac{\cos\omega}{n - \cos\omega} \tag{37}$$

The final expression for prism angle (α) is calculating by substituting the Eq. 38 in Eq. 37,

$$\cos\omega = \frac{f}{\sqrt{R^2 + f^2}} \tag{38}$$

$$\tan\alpha = \frac{R}{n\sqrt{R^2 + f^2} - f} \tag{39}$$

In imaging Fresnel lens, the flux concentration is measured by the f-number and defined as the ratio of the effective focal length to the diameter of the lens [131].

In a nonimaging Fresnel lens, the prime objective is to maximize the concentrating radiation rather than establish an image. Welford and Winston introduce the Edge ray principle for nonimaging optics [134]. According to this principle, the rays emitted from the source's edges will be redirected towards the receiver's edge, whereas rays come from the source's interior will end up on the receiver without generating an image. This principle permits the formation of a nonimaging lens with any combination of acceptance half angles (θ) in the cross-sectional plane and (ψ) in the plane perpendicular to it [131].

In 1999, Leutz et al. designed a nonimaging Fresnel lens for solar concentrators [141]. The design of a nonimaging lens depends on some critical parameters, including the β (prism angle), α (prism inclination angle), ±θ (cross-sectional acceptance half-angle pair), ±ψ (perpendicular acceptance half-angle pair), the angle (ω) that divides the aperture of the lens into the segments, and the refractive index (n) of the material. The solar radiations that reach the lens's outer surface at an angle smaller or equal to the acceptance half angles will be refracted to the receiver. The height of the lens above the receiver f (focal plane, exit aperture) can be calculated as shown in Eq. 40

$$f = \frac{d}{\tan\theta} \tag{40}$$

where d is the reference half-length of the receiver, and set as d = 1.0. From the reference point, the angles and positions of the primary prism to the right of the lens's optical axis are evaluated. All the succeeding prisms start when the last one is concluded. The width of the prism depends on the angle ω. The prism pitch in the x-direction and y-direction given by Eqs. 41,42

$$\Delta x = \cos(\beta - \alpha)\overline{BD}\ \omega \tag{41}$$

$$\Delta y = \Delta x \tan(\beta - \alpha) \tag{42}$$

where $\overline{BD}$ is calculated from the position of the previous prism. For the primary prism, the angle α is set at zero. Hence, with the two directions of incidence, two values for the β are found. Both prism angles β, are calculated by Newton's method in infinity loops, as shown in Eq. 43 [141].

$$|\beta_1 - \beta_2| < \Delta E \tag{43}$$

where ΔE is known as the error margin. The position of the prism is determined by the positioning vectors, as shown in Fig. 15. The position vectors define the centre point of the prism bottom in its position concerning either end of the absorber. Therefore, when both vectors pair are kept parallel, all the incident rays within the limit of acceptance half angles and the rays leaving the prism after refractions will hit the absorber with its outer limits. Eq. 44 gives the optimization criterion for Newton's method and the setting of the prism angle β.

$$\left| \frac{\overrightarrow{q}.x}{\overrightarrow{q}.y} - \frac{\overrightarrow{d}.x}{\overrightarrow{d}.y} \right| < \Delta E \tag{44}$$

The Eq. 44 is satisfied only when the inner infinity loop is broken, and the prism angle is set up. After the design of the 3D and 2D non-imaging concentrator, the theoretical geometrical concentration is defined from Eqs. 45 and 46 [131,141]

$$C_{3D} = \frac{n}{sin^2 \theta} \tag{45}$$

$$C_{2D} = \frac{n}{sin \theta} \tag{46}$$

The utilization of the Fresnel lens in solar-pumped laser is introduced by Yabe et al. to increase the output power and efficiency. In 2007, Yabe and the group employed the Fresnel lens for the first time to pump the Cr: Nd: YAG laser rod [22]. A significant improvement is found with an output power of 24.4 W, collection efficiency of 18.7 W/m^2, and solar to laser efficiency of 2.9% [22]. Liang and Almeida significantly advance the solar-powered laser beam brightness using a Fresnel lens (1.0 m) [98]. They successfully produced the 2.3 W CW TEM$_{00}$ (M$^2 \leq 1.1$) solar laser power with a 1.9 W laser beam brightness figure of merit, which is 6.6 times higher than the previous record [116]. For multimode operation, 8.1 W CW laser power is generated, corresponding to a 143%
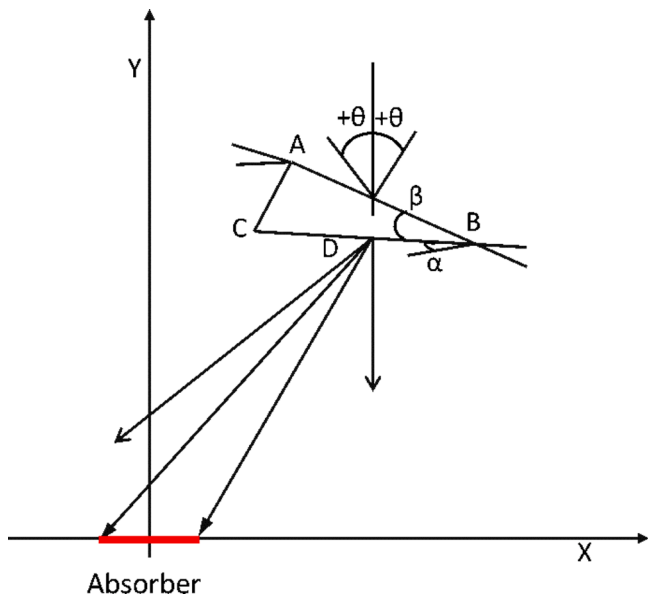

Fig. 15. Position of the prism in a Fresnel lens [131].

enhancement in collection efficiency [98].

4.2.3. Ring array concentrator

The utmost attainable solar concentration from a single reflective primary parabolic mirror is bounded by its aspect ratio. The achievable concentration of a single refractive Fresnel lens is also limited by its chromatic aberration. Hence, the scientific community suggested a ring-array concentrator (RAC) with a variable aspect ratio to reinforce solar energy research [142–146]. RAC combines the advantage of a parabolic mirror's reflective nature and a Fresnel lens's focusing method [145].

The ring array concentrator has come into consideration after the Pyreheliophoro, a form of solar concentrator in the 19th century [128, 147]. After that, Vasylev and Mouzouris continued research on ring array concentrators to improve solar concentration [148,149].

In 2018, Tibúrcio et al. proposed a compact pumping method to considerably improve the collection and conversion efficiency of an Nd: YAG solar laser by an innovative RAC [146]. Garcia et al. also demonstrated a simulated model of a 3D ring-array concentrator solar furnace [144]. The suggested system comprises five single-ring array concentrators forming a compact box-shaped solar furnace. In addition, compared to the medium size solar furnace, the 3D ring-array concentrator also presents an extensive tracking error correction capability. In 2021, Garcia and the group proposed an analytical and numerical analysis of a ring-array concentrator [145]. The presented RAC model is beneficial for designing future RACs of solar lasers.

The RAC employs the reflection and refraction processes of incident solar radiations through the surface of the parabolic ring mirror section and Fresnel lens, respectively. Fig. 16 illustrates the schematic diagram of a seven-ring RAC comprising parabolic mirror rings and a Fresnel lens. Each section of the parabolic mirror ring is mathematically sized and positioned to ensure no obstruction of the light path occurs [142, 145]. The focal spot is generated by the superposition of the concentrated solar radiations from the ring mirrors. The Fresnel lens is employed to focus the remaining central solar radiations toward the focus spot.

A parabolic ring is a section of a parabolic aspheric surface [145]. The sag equation for a generic geometric aspheric surface (z) is given in Eq. 47

$$z = \frac{c \times a^2}{1 + \sqrt{1 - (1 + k)c^2 a^2}} + \sum_{i=1}^{M} \alpha_i a^i = \frac{1}{2} \frac{a^2}{RoC} \tag{47}$$

where a is the radial coordinate, c is the curvature of the surface, and α is the aspheric coefficient. In the present case, the constant curvature k is -1 due to the pure parabolic configuration, and c is the inverse of the radius of curvature (c = 1/RoC). Eq. 48 is used to determine the radius of curvature (RoC$_n$) for a given nth ring with a desired focal length (h$_f$), inner aperture (a_{in_n}), and ring height modifier (h$_d$).

$$RoC_n = \sqrt{\left(h_f + (n-1)h_d\right)^2 - \left(a_{in_n}\right)^2} - \left(h_f + (n-1)h_d\right) \tag{48}$$

However, with h$_d$ > 0 mm, the vertical position of each inner ring increases linearly according to the ring number as shown in Eq. 49

$$\left(h_f + (n-1)h_d\right) \tag{49}$$

The entire RAC design depends on the initial parameter of the first ring. The primary procedure of RAC modelling is to define the outmost radial aperture of the first ring (a_{out_1}), which is also determines the maximum size of the RAC. The next step is to define the size of the first ring that is the width of the first ring (Δa_1) as shown in Eq. 50

$$\Delta a_1 = d_w \frac{a_{out_1}}{R} \tag{50}$$

where d$_w$ is the initial ring width and R is the base radius of the RAC. The inner radial aperture (a_{in_1}) can be found by subtracting the ring width from the outer radial aperture [145], as given in Eq. 51
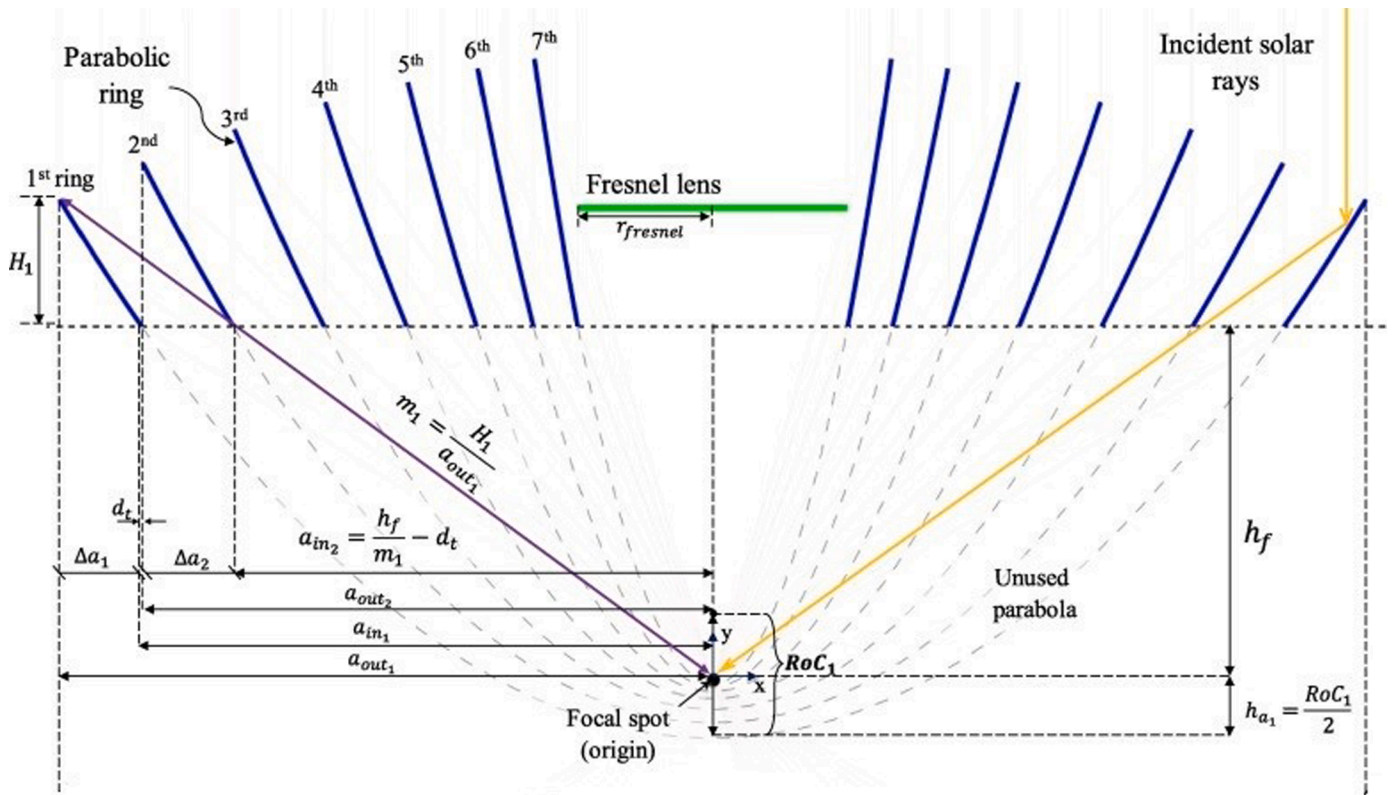
Fig. 16. Ring array concentrator unit with seven rings [145].

$$a_{in_1} = a_{out_1} - \Delta a_1 \tag{51}$$

The parabolic ring segment can be designed from both inner and outer radial apertures in the sag Eq. 47 [145]. In this, the vertex of the virtual parabolic sag will be positioned onto the origin point (0, 0), and its focal point at $(0, h_{a_1})$, as illustrated in Fig. 17 by the solid and dashed grey sag lines. The parabolic ring segment of the RAC model (solid blue sag line) is found by subtracting the h_{a_1} in Y-axis from the virtual parabola, which ensures the focus in the origin point.
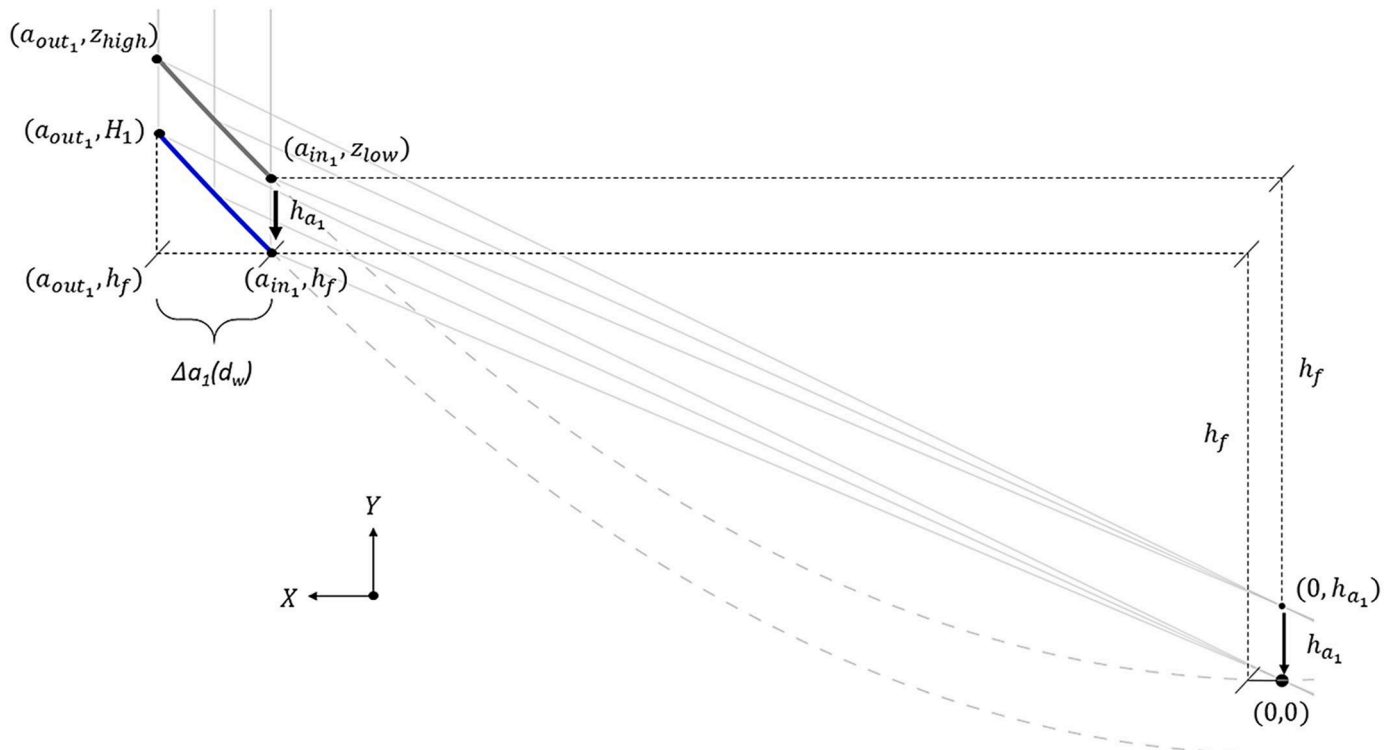
Fig. 17. Parametric positioning of the first parabolic ring [145].

The h_{a_n} is defined as the half of the radius of curvature of the ring as given in Eq. 52, and utilized to rectify the position of any n^{th} ring in the vertical axis. The height of the ring (H_n) is calculated from the Eq. 53

$$h_{a_n} = \frac{RoC_n}{2} \tag{52}$$

$$H_n = z_n - h_{a_n} \tag{53}$$

The outer radial aperture of the next ring is calculated by subtracting the ring thickness (d_t) from the inner radial aperture of the pervious ring as given in Eq. 54 [145]

$$a_{out_n} = a_{in_{n-1}} - d_t \tag{54}$$

To finalized the next ring, the inner radial aperture (a_{in_n}) can be found at the intersection of the reflected light ray from the top of the previous ring at ($a_{out_{n-1}}$, h_{n-1}) with reflected light ray from the top of the previous ring at with the focal length of the next ring at (XX, h_f+h_d), as given in Eq. 55 [145]

$$a_{in_n} = \frac{h_f + (n-1)h_d}{\frac{H_{n-1}}{a_{out_{n-1}}}} - d_t \tag{55}$$

A Fresnel lens is utilized to complete the remaining space. The radius of Fresnel lens is represented by $r_{Fresnel}$ as indicated in Eq. 56

$$r_{fresnel} = a_{in_N} \tag{56}$$

The height ($h_{Fresnel}$) of the Fresnel lens is depends on the interception of the reflected light ray from the top of the last ring (a_{out_N}, h_N) and the origin point with the position of the inner aperture of the last ring (a_{in_N}, YY), as given in Eq. 57 [145].

$$h_{fresnel} = \frac{H_N}{a_{out_N}} a_{in_N} \tag{57}$$

4.3. Secondary concentrator

Based on the sun-earth geometry, the concentrated intensity of the solar concentrator is confined to the sun image at the focal point, and there is a considerable mismatch between the shapes of the solar spot and laser medium [45]. Assume there are no more concentrators available to refocus the incident solar radiation. In such an instance, only the tiny area of the laser rod will be pumped to reach the lasing threshold, which is responsible for degrading the performance of solar lasers. Hence, the second concentrator is essential for lasing action.

4.3.1. Compound parabolic concentrator
The details of the Compound parabolic concentrator (CPC) began to appear in the literature from the mid-1960s in various contexts. The basic concept of CPC as a concentrator from Cerenkov counters is defined and developed by Hinterberger and Winston [150]. In 1966, Baranov et al. expressed the same principle of CPC in 3D geometry and proposed the 3D CPCs for collection of solar energy [151]. In 1974, the 2D geometry of CPC was characterized by Winston [129], and further, more detail of CPC has been described by Winston and Hinterberger [152] and Rabl and Winston [153].

The design of a non-imaging concentrator is based on the transporting of only edges of rays without the interior order, allowing attainment of the sine law of concentration limit [134]. The Second Law of Thermodynamics further supports the concentration limit, which states that heat cannot pass spontaneously from a colder to a hotter body. The natural flow of heat transport is always in the direction of increasing entropy. Rabl [138] examined this concentration limit very well from the thermodynamics approach. All the optical imaging design derives from Fermat's principle. In the same way, when Fermat's principle is applied to "strings" rather than rays, it gives the edge-ray algorithm of non-imaging optical design [134].

A CPC is a non-imaging concentrator comprised of two parabolas

segments (AB and A'B'). The CPC structure is classified into three parts: the planar entrance aperture (AA'), a totally internally reflecting side profile, and an exit aperture (BB'). The schematic diagram of CPC with string is shown in Fig. 18, in which one end of a string is connected to a rod tilted at an angle of θ to the aperture AA' and the second end to the edge of the exit aperture B'.

The string structure is extremely versatile and can be used with any convex absorber. By keeping the length of the string fixed, the profile of CPC can be expressed via moving the string from C to A'. The concentration ratio of 2D CPC is achieved from the following Eq. 58-61

$$AC + AB' = AB' + BB' \tag{58}$$

$$AC = AA' \sin\theta \tag{59}$$

$$AB' = AB' \tag{60}$$

$$C = \frac{AA'}{BB'} = \frac{1}{\sin\theta} \tag{61}$$

Rabl et al. proposed various absorbers to maximize solar energy collection [154]. These absorbers are divided as CPC with flat absorber, CPC with fin, CPC with "inverted vee" absorber, and CPC with the tubular absorber. However, the CPC with a flat absorber is most prominent because of its simplicity. Fig. 19 demonstrates the flat absorber and applies the edge-ray principle to evaluate the concentration ratio. All the incoming rays entering at the extreme collecting angle θ_i must exit via the rim point P' of the exit aperture. The meridian section restricts the solar rays to simplify the parabolic shape. If the concentrator is a 3D system, it must have an axis of symmetry; therefore, the reflecting surface is created by rotating the parabola around the concentrator axis. The symmetry determines the overall length of CPC, and the shape is completely described in terms of maximum input angle (θ_i) and diameter of the exit aperture (2a'). From the coordinate geometry, the focal length (f) of the parabola is calculated from Eq. 62

$$f = \frac{a'}{1 + \sin\theta_i} \tag{62}$$
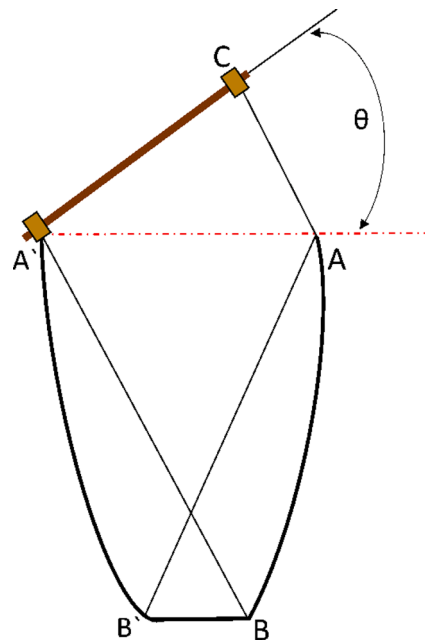
The overall length of the CPC is calculated by the Eq. 63

Fig. 18. Compound parabolic concentrator with string [134].
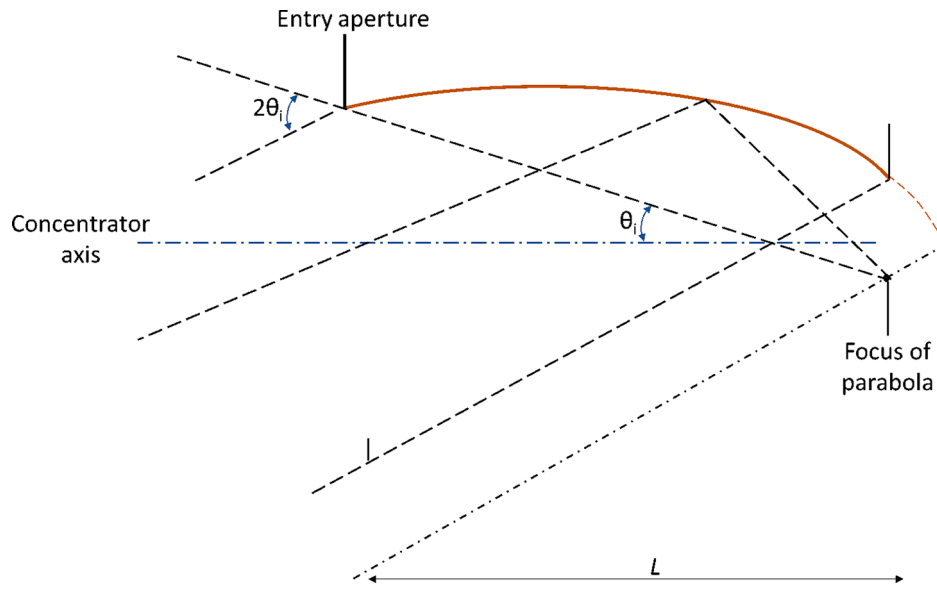
Fig. 19. Compound parabolic concentrator with flat absorber and applying the edge-ray principle [134].

$$L = \frac{a'(1 + \sin\theta_i)\cos\theta_i}{\sin^2\theta_i} \tag{63}$$

The entrance diameter of CPC is expressed by the Eq. 64

$$a = \frac{a'}{\sin\theta_i} \tag{64}$$

Based on Eq. 52, the total length of CPC is determined as Eq. 65

$$L = (a + a')\cot\theta_i \tag{65}$$

The main advantage of using a CPC is that it could offer a maximum theoretical concentration ratio, as expressed in Eq. 66

$$C = \frac{a}{a'} = \frac{1}{\sin\theta_i} \tag{66}$$

After the successful invention of solar lasers, the 2D CPC and 3D CPC have been used as secondary concentrators to focus the concentrated solar radiations at the laser rod. The 2D CPC was first introduced by Weksler et al. in 1988 [65]. However, the output power of the solar laser was merely 60 W with a collection efficiency of 1.56 W/m². In 2013, Lando et al. conducted side-pumped solar laser experiments in low and high pumping density regimes. A segmented primary mirror is utilized to focus the solar radiation towards a stationary non-imaging-optics secondary concentrator, which illuminated a Nd: YAG laser rod [95]. The proposed low-density system consists of a 2D CPC to pump a Nd: YAG laser rod that generates an output power of 46 W. The presented high-density system consists of a 3D CPC followed by a 2D CPC to pump the Nd: YAG laser rod, which produces an output power of 45 W with a collection efficiency of 6.7 W/m² [95]. In 2015, a significant advance in solar-pumped laser beam brightness was obtained by pumping the 3 mm diameter Nd: YAG single-crystal rod with a heliostat-parabolic mirror system [122]. However, to further compress the concentrated solar radiation into the laser rod within a V-shaped pumping cavity, a rectangular fused silica light guide and a 2D-CPC concentrator are combined. The proposed system with 2D-CPC produces the 4.4 W continuous-wave TEM$_{00}$ mode (M²≤1.05) solar laser power with a 4.0 W laser beam brightness figure of merit [122].

4.3.2. Dielectric totally internally reflecting concentrator

In 1986, the concept of the dielectric totally internally reflecting concentrator was introduced [155]. DTIRC contains three parts: a curved front surface, a totally reflecting side profile, and an exit aperture. The combination of refraction on the front surface and TIR from the sidewall enhances the concentration of DTIRC, which is close to the theoretical maximum limits [129]. Due to the curved front surface and larger refractive index of dielectric, DTIRC has the advantage of a high concentration ratio [130].

Ning et al. developed two design methods for the DTIRC; the maximum concentration method and the phase conserving method [156]. Both design strategies produce the same structure. However, the primary method offers a slightly higher concentrator with an edge ray solution incorporating TIR. In the phase conversing method, the reflecting rays are parallel to one another with a direction corresponding to the line from P$_2$ to P`$_3$. The exiting extreme rays are reflected from the portion between P$_2$ and P$_3$ that forms a new wavefront.

The schematic diagram of DTIRC is shown in Fig. 20. The incoming rays within the acceptance angle reach the exit aperture. The incident solar radiations beyond the acceptance angle will eventually exit from the side profile. Thus, the incident rays at the acceptance angle are called extreme rays, and they play a vital role in identifying the side profile of the concentrator. For the simplicity of the design, the front
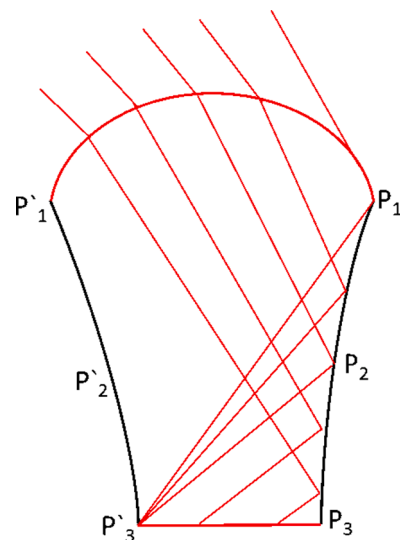

Fig. 20. Schematic diagram of dielectric totally internally reflecting concentrator [130].

surface of DTIRC is considered a portion of the sphere, and side portions are divided into upper and lower parts. The upper profile consists of the P_1 to P_2, and the lower profile covers the P_2 to P_3. After a single TIR, the extreme rays between P_1 to $P_2$are directed to the corner $P`_3$. The ray hitting $P_2$ only satisfied the TIR and exited from $P`_3$. The refractive index is not high enough between P_2 and P_3 to reflect the extreme rays to $P`_3$.

Hence, the extreme rays reflected from the upper part (P_1, P_2) of the profile converge onto a point and rays from the lower portion (P_2, P_3) exit in parallel. Fermat's principle can be used to create the coordinates of the side profile. As illustrated in Fig. 21, the total path length of the ray from the entrance to the exit is divided into four parts and named l_1, l_2, l_3, and l_4. According to Fermat's principle, the total optical path length is constant for every ray connecting the initial and final wavefront, as shown in Eq. 67 [154,155]

$$\int n \, ds = l_1 + n(l_2 + l_3 + l_4) = Const. \tag{67}$$

where l_1 is the length from the point on the initial wavefront to the surface of the DTIRC, l_2 is from there to the reflection point, l_3 is from the reflection point to the exit of DTIRC, and l_4 is from the exit of DTIRC to the final wavefront. Combining Eq. 67 with DTIRC height and length constraints, the parameters l_1, l_2, l_3, and l_4 can be solved. Then the profile coordinates of the concentrator can be determined analytically.

The design parameters of DTIRC are related to the radius of curvature (R), optical path length (C), and height (H) of DTIRC. The radius of curvature is calculated in terms of entrance diameter (d_1) and front surface arc angle (φ) from Eq. 68

$$R = \frac{d_1}{2 sin\varphi} \tag{68}$$

The height of DTIRC is calculated from the entrance diameter (d_1) and exit diameter (d_0), as shown in Eq. 69

$$H = \frac{1}{2}(d_1 + d_0)\cot\theta \tag{69}$$

The optical path length is calculated as shown in Eq. 70 [155]

$$C = 2Rsin^2[(\theta_a + \varphi)/2] + n (d_1 + d_0)/[2 sin(\theta)] \tag{70}$$

Where θ_a is the acceptance angle and θ is an arc angle. The rays which
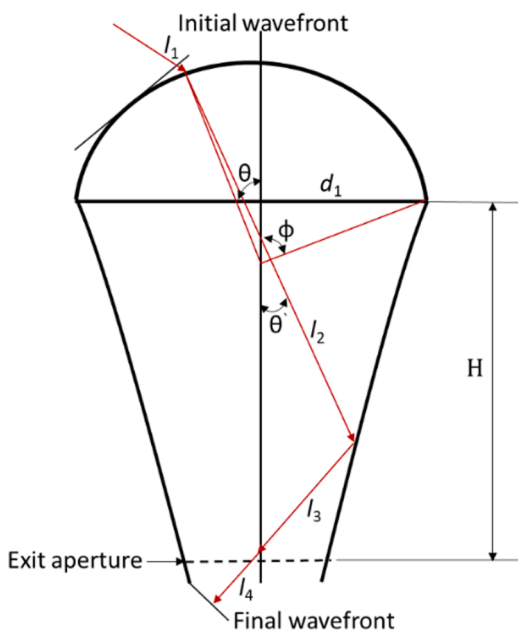

Fig. 21. Typical optical path of dielectric totally internally reflecting concentrator consists of four parts: l_1, l_2, l_3, and l_4 [157].

are from P_1 to $P`_3$ only satisfy the TIR condition at P_2, and the exit angle is expressed as shown in Eq. 71

$$\theta_0 = \pi - \theta - 2\theta_c \tag{71}$$

where θ_c is a TIR critical. After solving the equations for l_2, l_3, and l_4 the x and y coordinates are calculated from the phase conversing method as shown in Eqs. 72 and 73 [155]

$$x = R \sin(\theta) + l_2\sin(\theta') \tag{72}$$

$$y = H - l_2\cos(\theta') + R[\cos(\theta) - \cot(\varphi)] \tag{73}$$

However, the maximum concentration method does not need rays hitting a portion P_2, P_3 of the side profile exiting with the same angle. The methodology is identical for the rays hitting the upper portion of DTIRC for both maximum concentration and phase conserving methods. Therefore, the derived formulas of R, H and C for the upper portion are also the same for the maximum concentration method. However, much attention is given to the lower part because there is no longer a clearly defined wavefront. Assume that a point in the part P_2, P_3 has been determined with coordinates (X_i, Y_i). The next point (X_{i+1}, Y_{i+1},) is just the intersection of the next extreme ray with a straight line extending from (X_i, Y_i) with a slope that causes this ray to be completely internally reflected. The following recursion relations can be used to prove that (X_{i+1}, Y_{i+1}) is connected to (X_i, Y_i) [157].

$$X_{i+1} = \frac{H + R\sin(\theta) - Y_i + X_i\tan(\theta_c + \theta') - R\sin(\theta)\cot(\theta')}{[\tan(\theta_c + \theta') - \cot(\theta')]} \tag{74}$$

$$Y_{i+1} = (X_{i+1} - X_i)\tan(\theta_c + \theta') + Y_i \tag{75}$$

The disadvantage of a DTIRC is that it cannot efficiently transfer all of the solar energy which is collected into a lower index media [130].

The DTIRC was used initially for photovoltaic applications. In 2011, Liang et al. employed a modified version of the DTIRC to efficiently concentrate the solar radiations from the focal zone to the thin rod [25]. The achieved power from the superior light collection and concentration capability of the DTIRC and the small conical pumping cavity was 12.3 W, corresponding to the collection efficiency of 19.3 W/m².

4.3.3. Light guide system

Several types of light guide systems have been proposed, including hollow reflective light guides [158,159], prism light guides [160,161], dielectric light guides, i.e., solid or fluid-filled light guides [162,163], and lens guides [164,165] for transmission of light beams.

In 1986, Johnson and Selkowitz developed an optical theory of light guide systems, which is utilized to determine the design specifications of a light guide system [158]. The design of a light guide system begins with an initial specification that defines specific fixed material, structural and optical parameters of the system [158] . The selected material of the light guide introduced the optical properties such as surface reflectance, refractive index etc., in the system. The prime structural design specification is the light guide length.

The design specifications also include the collector's tracking accuracy and its transmittance. The fraction of the light guide's output flux that reaches the illuminated area is known as the coefficient of utilization (CU). Apart from the fixed design parameters, two free design parameters, the light guide aperture area ($A_{light\ guide}$) and the collector aperture area ($A_{collector}$), are determined to satisfy particular design constraints. Fig. 22 illustrates the schematic diagram of light guide.

The required flux output (Φ_{output}) is determined from the floor area ($A_{distributed}$) over which the flux is distributed, desired flux density level ($E_{distributed}$), and the coefficient of utilization as shown in Eq. 76

$$\Phi_{output} = A_{distributed} \ E_{distributed} / CU \tag{76}$$

Solar insolation is calculated using flux density or the sun's luminance (L_{sun}). The direct normal flux density (E_{sun}) is calculated from L_{sun}
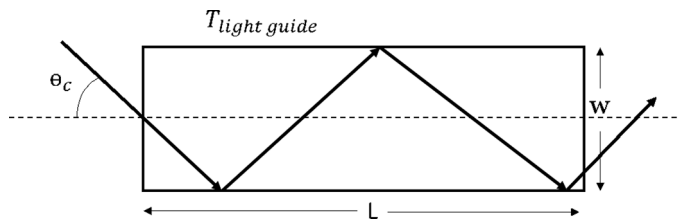
Fig. 22. Schematic representation of light guide.

(in candelas per square foot) and the sun's angular radius as given in Eq. 77

$$E_{sun} = L_{sun} \ \pi \sin^2\theta_{sun} \ (\theta_{sun} = 0.27°) \tag{77}$$

It is assumed that the collector's ray transmittance ($T_{collector}$) is uniform and equal to a fixed value; also, the collector's tracking error is negligible, so the collector's output beam is stationary. Thus, the beam that is fed into the light guide is stationary and has a uniform luminance, as given in Eq. 78

$$L_{input} = T_{collector} \ L_{sun} \tag{78}$$

If the beam's size, shape and luminesce is known, then the output flux is calculated. The amount of the flux (Φ_{input}) that enters into the light guide is determined by Eq. 79

$$\Phi_{input} = \Phi_{output} \ / T_{light \ guide} \tag{79}$$

Taking into consideration the collector transmittance, solar flux ($\Phi_{collected}$) is determined by Eq. 80

$$\Phi_{collected} = \Phi_{input} \ / T_{collector} \tag{80}$$

To know how much flux is collected, the collector area is calculated as given in Eq. 81

$$A_{collector} = \Phi_{collected} \ / E_{sun} \tag{81}$$

where E_{Sun} is the incident solar flux density, which may be specified or may be determined from the sun luminance L_{Sun} by using Eq. 77. The output flux (Φ_{output}) is determined from the light guide's input flux (Φ_{input}) and flux transmittance ($T_{light \ guide}$) as given in Eq. 82

$$\Phi_{output} = T_{light \ guide} \ \Phi_{input} \tag{82}$$

Eq. 82 can also be rewritten in terms of the specified output flux as given in Eq. 83 [158]

$$\Phi_{output} = T_{light \ guide} \ L_{input} \ \pi \mathscr{A}(\tau_{min}) \tag{83}$$

where $\mathscr{A}$ depends on the specific type of light guide system that is being analyzed (e.g., square-section hollow reflective, circular-section dielectric, etc.). $\mathscr{A}$ is implicitly a function of the light guide's design parameters (aperture dimension, wall reflectance, etc.). $\mathscr{A}$ has units of area. $\mathscr{A}(\tau)$ is defined for any ray transmittance value, τ, from zero to τ_{max}, where τ_{max} is the light guide's maximum ray transmittance.

The light guide's characteristic function, $\mathscr{A}$, also determines its flux transmittance, $T_{light \ guide}$, as given in Eq. 84 [158]

$$T_{light \ guide} = \tau_{min} + \left(\frac{1}{\mathscr{A}(\tau_{min})}\right) \int_{\tau_{max}}^{\tau_{min}} \mathscr{A}(\tau) d\tau \tag{84}$$

In solar-powered lasers, the fused silica light guide is employed to homogenize the pump light. The fused silica material has the advantage of a low coefficient of thermal expansion and a wide transparency range [59]. In 2017, Bouadjemine et al. improved the output beam stability of a TEM_{00} mode solar laser via a twisted fused silica light-guide [125]. The twisted light guide is utilized to obtain uniform pumping along the Nd: YAG laser rod. The achieved output power from the proposed solar-powered laser is 2.3 W, corresponding to a collection efficiency of

1.96 W/m^2.

In solar-powered lasers, the liquid light guide works as a lens. In 2018, Liang et al. attained a study of Cr: Nd: YAG solar laser based on the fused silica liquid light guide lens that shows an enormous output power of 32.5 W with a collection efficiency of 32.5 W/m^2 [53]. In 2019, Vistas et al. produced a doughnut-shaped solar laser beam [91]. The proposed system consists of a fused silica liquid light guide lens and a conical pump cavity, within which an Nd: YAG single-crystal rod is efficiently end-side pumped. The presented solar-powered laser produces the multimode solar laser power of 24 W and 6.4% slope efficiency.

4.3.4. Aspheric lens

With recent developments, aspherical lenses are a go to solution for any high-performance optical system. Carl Zeiss introduced the first aspherical lens, named as the Katral lens followed by the Volk conoid lens by David Volk [167,168] . In 1980, Whitney et al patented their first aspheric system, termed as the Fulvue aspheric blended lenticular lens system. Such lenses are engineered to correct aperture dependent aberrations, field dependent aberrations, reduction of weight, localizing a system etc. [169]. For example, in applications involving space borne instruments, systems are preferred to be compact and light weight. Hence, using the aspheric design is of tremendous importance. The schematic diagram of aspheric lens with design parameters is shown in Fig. 23. The standard equation for any aspheric surface is

$$z = \frac{\frac{r^2}{R}}{1 + \sqrt{1 - (1+k)\left(\frac{r^2}{R^2}\right)}} + \sum_{n=2}^{m} A_{2n} r^{2n} \tag{85}$$

where r=radial coordinate, Z=sag, R= vertex radius of the curvature.

$$K = \begin{cases} < -1, & for \ hyperbolas \\ -1, & for \ parabolas \\ \in (-1, 0), & for \ oblate \ ellipse \\ 0, & for \ spheres \\ > 0, & for \ prolate \ ellipses \end{cases}$$

The $A_{2n} r^{2n}$ term refers to higher order aspheric, as given in Eq. 86

$$A_{2n} r^{2n} = A_4 r^4 + A_6 r^6 + A_8 r^6 + \dots \tag{86}$$

Usually, higher order aspheres play a vital role in performance enhancement with very low-cost increase. Optimizing an aspheric lens involves increasing number of field points and aperture size to control higher order polynomials. Unlike freeform surfaces, aspherics have an axis and are rotationally variant. The aspheric equations usually help to
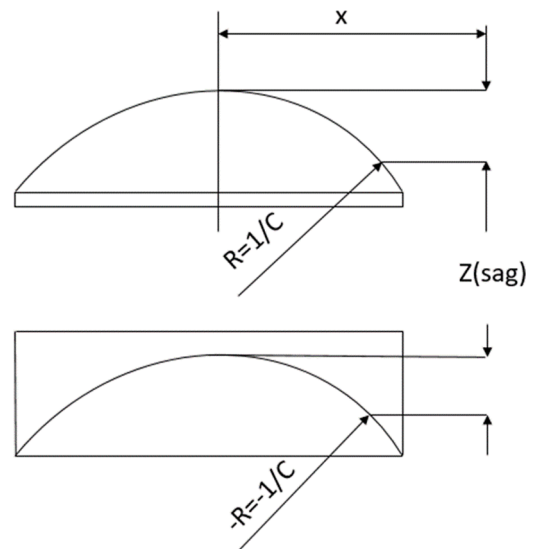

Fig. 23. Schematic diagram of aspheric lens with design parameters.

nullify different sets of aberrations. This is followed by a suitable manufacturing process and metrology [170,171] .

Based on the state-of-the-art of solar-pumped solid-state lasers (Table 2) in subsection 3.5, the fused silica aspheric lens is the most prominent second concentrator in solar-powered lasers after the light guide lens. In 2014, by employing the Fresnel and the aspheric lens as solar concentrators, the performance of the solar-powered laser was improved with an output power of 59.1 W and a collection efficiency of 14.67 W/m^2 [118]. Liang and the group utilized a large fused silica aspheric lens for an efficient focusing of the concentrated solar power from the focal zone of the parabolic mirror into the laser rod mounted within a novel two-dimensional semi-cylindrical pump cavity [39]. The side-pumped solar laser produced a 15.3 W continuous-wave solar laser power with 5.4% slope efficiency and 2.43% solar-to-laser conversion efficiency. Recently, a Ce: Nd: YAG solar-powered laser was presented that used a fused silica aspheric lens that coupled the concentrated solar radiation from the focal zone of a parabolic mirror. The obtained output power from the solar laser is 11.2 W, corresponding to the solar-to-laser power conversion efficiency of 4.50% [60]. The most recent research on Ce: Nd: YAG laser also comprised a fused silica aspheric lens that focused the concentrated solar radiations from the primary parabolic mirror into three laser rods. The proposed solar-powered lasers generate an output power of 16.5 W with 41.25 W/m^2 of collection efficiency [63].

4.4. Tertiary concentrator

Tertiary concentrators are essential for high-flux pumping of the laser medium. In solar-powered lasers, numerous tertiary concentrators such as 2D CPC [98], conical mirrors [123], 2D V-shaped cavities [166] and semi-cylindrical mirrors [39] are utilized to compress the concentrated solar radiation from their input aperture to the laser-active medium.

In the year 2013, Liang and Almeida proposed the novel TEM$_{00}$ solar laser system composed of the first-stage Fresnel lens, the second-stage fused silica aspheric lens and the third-stage 2D-CPC concentrator [98]. The third-stage 2D-CPC concentrator has a large rectangular input aperture and a narrow rectangular output aperture, as shown in the Fig. 24. The presented 2D-CPC is employed to convert the rays from large-aperture emitting into a small angle to small-aperture emitting into a large angle; thus, the source étendue is preserved. This preservation indicates that irradiance is larger at the output aperture than at the entrance aperture, leading to a net concentration of the pump radiation [98]. In the end, the solar-powered laser produces the 2.3 W CW TEM$_{00}$ (M$^2 \leq 1.1$) solar laser power with a 1.9 W laser beam brightness
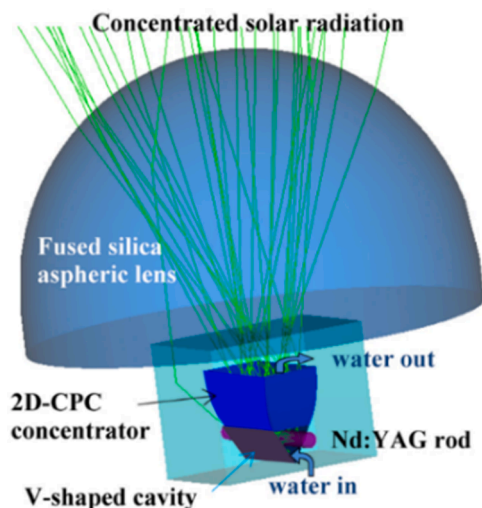
figure of merit. In the case of multimode operation, 8.1 W CW laser power is achieved, corresponding to a 143% enhancement in collection efficiency.

In the year 2017, Bouadjemine et al. utilized the 2D-CPC/2V-shaped pump cavity to pump the thin laser rod efficiently. The authors improved the output beam stability of a TEM$_{00}$-mode solar-pumped laser by coupling the concentrating solar power at the focal spot of a primary parabolic mirror to the entrance aperture of a 2D-CPC/2V-shaped pump cavity [125]. The proposed solar laser produces the 2.3 W continuous-wave TEM$_{00}$-mode laser power, corresponding to 1.96 W/m^2 collection efficiency and 2.2 W laser beam brightness figure of merit.

In 2020, a compact side-pumped solar laser design was proposed to improve the TEM$_{00}$-mode solar laser output performance substantially [166]. As illustrated in the Fig. 25, the laser system consists of a rectangular hollow pipe and a 2V-shaped dry pump cavity to couple and redistribute the concentrated solar radiation from the focal zone of a parabolic mirror to a grooved Nd: YAG rod. Maximum TEM$_{00}$-mode solar laser power of 32 W is numerically calculated for a grooved Nd: YAG rod, corresponding to 10.7 W/m^2 collection efficiency. The laser beam brightness figure of merit of 31.4 W is also numerically attained. The proposed laser head scheme has a simpler and more compact design than previous schemes.

Liang and the group also proposed a novel two-dimensional semi-cylindrical pump cavity [39]. The presented solar-powered laser consists of an aspheric fused silica lens that effectively focuses concentrated solar pump power from the focal zone of the parabolic mirror into the thin laser rod mounted within the two-dimensional semicylindrical pump cavity. The authors experimentally calculated the 15.3 W CW solar laser power, corresponding to 17.0 W/m^2 collection efficiency, 5.40% slope efficiency and 2.43% solar-to-laser power conversion efficiency.

Liang et al. reported the first simultaneous emission of three CW solar laser beams by end-side-pumping three Nd: YAG laser rods within a single conical pump cavity [108]. The conical pump cavity serves as a tertiary concentrator. The secondary aspheric fused silica lens is utilized to couple the concentrated solar radiation from the parabolic mirror into the laser rods within the conical pump cavity. The presented solar-powered laser produces 18.3 W multimode solar laser power, resulting in 5.1% laser slope efficiency and 0.036 W laser beam brightness figure of merit [108].

5. Active medium

A laser crystal for solar-powered lasers should have a high ratio of fluorescence lifespan to the pulsed threshold, operate at about room
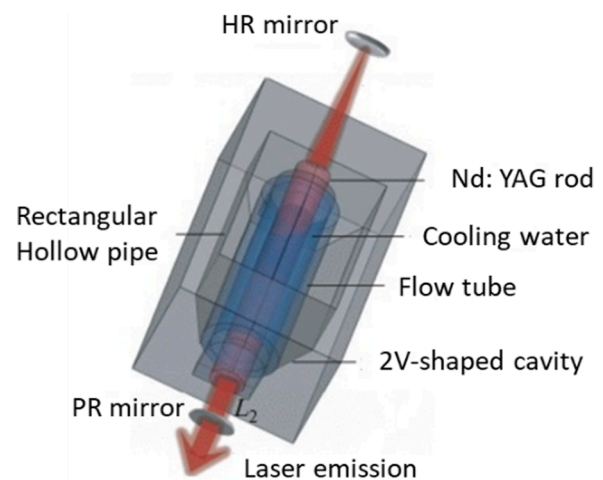

Fig. 24. 3D view of the solar laser head with 2D-CPC and V-shaped cavity [98].

Fig. 25. Schematic diagram of the solar laser head with 2V-shaped cavity [166].

temperature to ease heat rejection, emit at a wavelength suitable with a good detector, and be mechanically robust [37]. If the appropriate laser material is found, a solar laser can produce intense coherent radiation. This section is divided into two parts; the first part discusses the Nd: YAG laser rod and co-doping of Ce and Cr, and the second part details the pumping methods of the active medium.

5.1. Nd: YAG laser rod

Neodymium doped yttrium aluminium garnet (Nd: YAG) is a crystal prevailing as a lasing medium for solar-powered solid-state lasers. The YAG lattice has various properties that make it an effective laser host material, including stability, hardness, high quantum efficiency, and optically isotropic [157]. In 1964, Nd: YAG crystal's laser operation was first explained by Geusic et al. at Bell Laboratories. The Nd: YAG is created by substituting a tiny quantity of yttrium ions in the YAG crystal structure with triply ionized neodymium that works as a dopant. These crystals are grown by the Czochralski technique [157]. The yttrium ions are replaced with neodymium because of the same size. The details of the Nd: YAG crystal is provided in Section 2.3.1.

To enhance the performance of the solar lasers, the first factor is that there should be an excellent spectral match between the emission spectrum of the solar radiation and the absorption spectrum of the laser material. Since the first solar-powered solid-state laser, Nd: YAG rod has been indicated as the best active medium. However, to extend the absorption of the sunlight spectrum in the active medium, Cr is co-doped into the Nd: YAG material. Because the sensitizer Cr^{3+} ions have broad absorption bands in the visible region, which match the solar spectrum [66].

Recently, the Ce: Nd: YAG rod has been employed for an efficient solar to laser power conversion efficiency [50,62]. The results of the Ce: Nd: YAG rod were compared with that of the Nd: YAG rod, and the solar to laser power conversion efficiency was 1.57 times better than that of the Nd: YAG laser rod [62]. Because the absorption spectra of Nd: YAG has several narrow bands extending to visible wavelength, which results in a relatively low overall efficiency. However, the Ce: Nd: YAG absorption spectrum has two broad absorption bands (centred at 340 and 460 nm) in the visible range overlapping with the incident solar radiations [157]. Thus, the Ce: Nd: YAG ceramic can be a suitable laser medium for solar-pumped lasers due to its large absorption cross-section in the visible spectral range that matches the sunlight spectrum.

However, solid-state active materials have two serious factors that limit the output power; the first is the scattering and absorption losses, and the second is the thermal lens effect [44]. The scattering and absorption losses are occurred due to the imperfection of the laser host material and from impurities contained in the raw material for the laser host. These losses can be minimized with material preparation technology. The Nd: YAG crystal is pumped strongly because of the high threshold pumping intensity. Thus, the laser material is heated to extremely high temperatures by high-pumping radiation. When the material is cooled with a coolant (water), the temperature difference between the laser rod axis and the periphery is considerable. This temperature difference causes the thermal lens effect of the solid-state laser material that decreases the lasing efficiency and the beam quality. Significant research efforts have occurred over Nd: YAG rod for heat management in the laser medium [99,127,172]. The scientific community attained various research regarding side-pumping and multirod pumping methods for heat management [41,106–111]. The multirod pumping distributes the concentrated solar radiation among multiple rods that reduces the heat load, temperature, and stress intensity. In the year 2022, researchers reported the most efficient simultaneous emissions of three continuous-wave solar laser beams within a single conical pump cavity. For 356 W incident solar power, 16.5 W continuous-wave total multimode Ce: Nd: YAG solar-powered laser power is evaluated, corresponding to 4.64% solar-to-laser conversion efficiency, 41.25 W/m^2 collection efficiency, and 7.64% slope efficiency [63]. Costa and

the group numerically studied the multi-rod solar laser end-side pumping concept to improve the TEM_{00} mode solar laser output power level and beam brightness through a zigzag beam merging technique [113]. The laser beam merging technique provides a better overlap between the pump and the fundamental mode volumes. The authors successfully calculate the total TEM_{00} mode laser power from 37 laser beams of 5.2 kW with the highest beam brightness figure of merit of 148 W [113].

In 2014, a comparative study was also conducted based on the different laser rods (polished, unpolished, grooved) by keeping the other parameters of the laser medium constant. The polished rod is installed inside the cavity and filled with water. However, the lowest output power is obtained from the polished rod because the interface is smallest between the polished rod and cooling water [99]. Thus, unpolished and grooved rods have better heat dissipation in solar-powered lasers. Among the unpolished and grooved rods, the grooved rod had the highest output power because of two possible factors. The first factor is the large side surface of the rod, which can receive more pumping light in the laser cavity. Another factor is the large interface of rod and water, which offers better heat dissipation and reduces the thermal lens effect [99]. In 2018, Almeida et al. produced the first emission of a doughnut-shaped solar laser beam from a side-pumped grooved Nd: YAG laser rod by NOVA heliostat-parabolic mirror solar energy collection and concentration system [92]. A double-stage semi-spherical lens/2D-trapezoidal-shaped pumping cavity is utilized to efficiently couple and redistribute the concentrated solar pump light from the focal zone of a parabolic mirror (1.5 m) to a 4.0 mm diameter, 34 mm length, 1.0 at.% grooved Nd: YAG rod. The laser system produces the 3.0 W doughnut-shaped solar laser beam with a long asymmetric laser resonator, without adding any extra optical phase element in the resonator [92].

5.2. Pumping methods

Laser pumping is the process of energy transfer from concentrated solar radiations to the Nd: YAG rod to excite the electrons from a lower energy state to a higher energy state [173]. In solar lasers, the pumping process is broadly classified as side pumping and end pumping, as shown in Figs. 26 and 27 [174].

The end pumping method is more effective than the side pumping. But the side pumping provides a uniform absorption along the rod axis, thereby reducing the thermal loading effects.

The beam quality of solar laser is also from the side-pumping configuration. A side-pumping technique is also thought to be more convenient than an end pumping for scaling reasons. The combination of
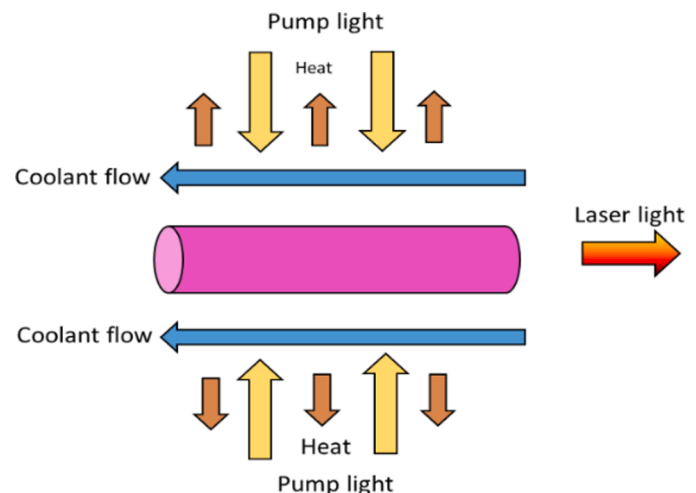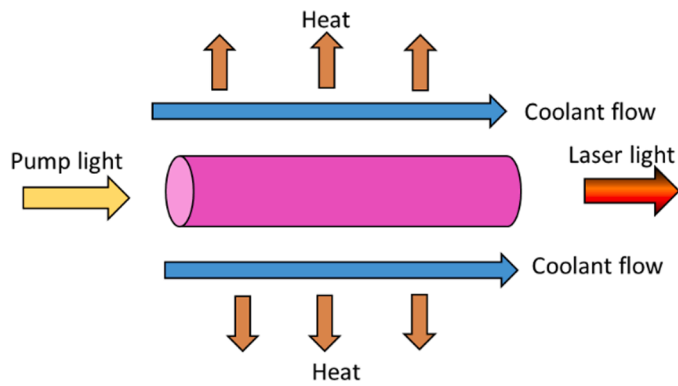

Fig. 26. Side-pumping method.

Fig. 27. End-pumping method.

both end pumping and side pumping methods is also an efficient configuration known as an end-side or hybrid scheme [106].

5.2.1. Side pumping method

Side pumping is an optical pumping technique for a laser gain medium in which the pump light is introduced from the side, i.e., in a path nearly perpendicular to the laser beam. Fig. 28 illustrates the side pumping method in which the pump light is distributed around the cylindrical rod. For an Nd: YAG laser rod with thermal conductivity (K), the heat is uniformly produced at A_0 per unit volume, and the steady-state temperature at any point along a radius of length (r) is expressed in Eq. 87 [175]

$$T(r) = T_0 - \frac{A_0 \, r^2}{4K} \tag{87}$$

where T_0 is the temperature at the centre of the rod. The A_0 is defined from the Eq. 88

$$A_0 = \frac{P_a}{\pi r_0^2 L} \tag{88}$$

where P_a is the dissipated power in the crystal, L is the length, and r is the radius of the rod, respectively. The heat generated in the laser rod is directly proportional to input power. Hence, from Eqs. 87 and 88, the thermal radial gradient is introduced as the radial variation of the refractive index. This change of refractive index is separated into a stress-dependent variation $(\Delta n(r)_T)$ and temperature-dependent variation $(\Delta n(r)_\epsilon)$, as shown in Eq. 89 [106]

$$n(r) = n_0 + \Delta n(r)_T + \Delta n(r)_\epsilon \tag{89}$$

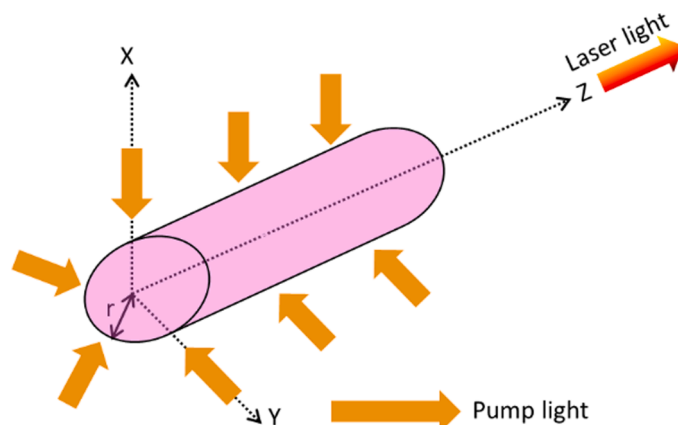where n(r) is the radial variation of the refractive index, and n_o is the

refractive index at the centre of the rod. Thus from the side pumping method, a thermal radial change is created in the Nd: YAG rod that leads to the distortions of the laser beam.

The side-pumping approaches are suitable for producing high-quality solar laser beams in the TEM$_{00}$ mode [114]. Because the side-pumping configuration provides a more uniform pump absorption profile along the laser rod. Compared to the end-side-pumping approach, the solar laser beam brightness from a side-pumping approach is usually much higher [39]. Another benefit of the side-pumped solar laser is its better solar tracking error compensation capabilities. In 2019, Liang and the group reported significant progress in the slope efficiency of solar lasers by the side-pumping method. A 3.0 mm diameter, 30 mm length Nd: YAG single-crystal laser rod is side pumped via a heliostat-parabolic mirror [39]. The side-pumped solar lasers generate 15.3 W continuous-wave laser power, resulting in 5.40% slope efficiency and 2.43% solar-to-laser conversion efficiency. The achieved slope efficiency is 1.08 times more than the previous record with Nd: YAG single-crystal rod by end-side-pumping approach [54]. In 2021, Vistas et al. advanced the performance of the Ce: Nd: YAG solar-powered laser by using a side-pumping configuration [62]. The authors also compared the output performance of a Ce: Nd: YAG laser rod (4.0 mm diameter, 35 mm length) with an Nd: YAG laser rod (4.0 mm diameter, 35 mm length). From the incoming solar power of 600 W, the Ce: Nd: YAG solar laser produces 23.6 W/m^2 collection efficiency, 4.4% slope efficiency, and 2.8% solar-to-laser power conversion efficiency, which are 1.57, 1.47, and 1.56 times, respectively, higher than the Nd: YAG laser rod [62]. The authors concluded that the Ce: Nd: YAG ceramic rod has great potential for enhancing the efficiency of side-pumped solar lasers.

5.2.2. End pumping method

The pump light is distributed nonuniformly in the end pumping method. Heat deposition becomes inhomogeneous due to the transmission of concentrated solar radiations only at the end of the laser rod. Fig. 29 illustrates a laser rod pumped by end pumping scheme.

The non-uniform temperature distribution and inhomogeneous local heating in the Nd: YAG crystal degrades the beam quality [175]. An end-pumped Nd: YAG rod has a temperature profile that accompanies pump light distribution across the pumped region. The temperature is decayed from the edge of the pumped region to the cooled cylindrical surface of the rod. By assuming consistent cooling on the laser rod's surface, which implies that the temperature at each point along the axis of the rod is constant, a differential equation for thermal transfer in a cylindrical rod is expressed in Eq. 90 [175].

$$\frac{1}{r}\frac{\partial}{\partial r}\left[r\frac{\partial T(r,z)}{\partial r}\right] + \frac{\partial^2 T(r,z)}{\partial z^2} = -\frac{Q(r,z)}{K_c} \tag{90}$$

where Q (r, z) is the heat in unit volume, K_c is the thermal conductivity (W/m .K), and T(r, z) is the temperature as the function of radial
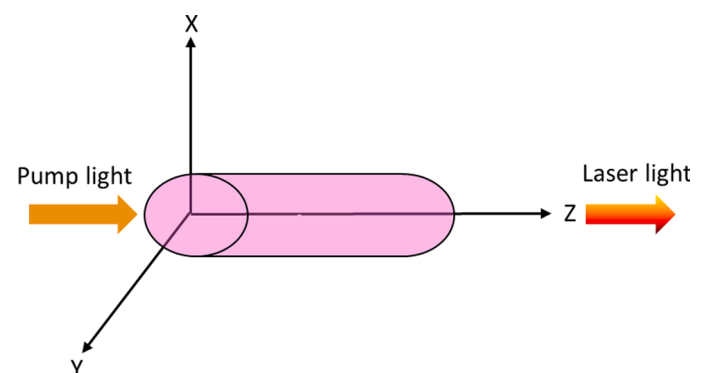

Fig. 28. Side-pumping of a Nd: YAG laser rod [173].

Fig. 29. End-pumping of a Nd: YAG laser rod [173].

distance (r) and position along the z-axis.

Thermal distribution inside an Nd: YAG material is a function of absorbed power density. According to the law of absorption, the intensity of pumping light decreases along the z-axis, and Q(r, z) are expressed in various ways depending on the beam shape, such as flat hat, top hat, Gaussian, or super-Gaussian [176]. The inhomogeneous heat deposition in end-pumped solar-powered laser systems leads to crucial thermal changes in the laser rod, resulting in complex refractive index variations. As shown in Eq. 91, the change in the refractive index is divided into two parts.

$$n(r,z) = n_0 + \Delta n(r,z)_T + \Delta n(r,z)_\varepsilon \qquad (91)$$

where n(r, z) is the total index of refraction, $\Delta n(r, z)_T$ is the first part of the refractive index related to temperature, $\Delta n(r, z)_\varepsilon$ is the second part of refractive index related to stress, and n_0 is the refractive index of a material. Due to the significant fluctuation in the refractive index, the optical distortion arises, which can degrade the optical quality of the laser beam and also limit the laser output power [106].

In 2007, Yabe et al. developed a solar laser with an end-pumped configuration [22]. However, the output power from the Cr: Nd: YAG solar-powered was 24.4 W due to the thermal changes in the laser rod. The majority of solar laser efficiency improvements have been made using the end-side-pumping method [91]. The solar laser collection efficiency of 32.5 W/m^2 is obtained by end-side-pumping a 4.5 mm diameter, 35 mm length, Cr: Nd: YAG laser rod by a heliostat-parabolic mirror system [53]. Another critical issue for the solar laser is the brightness figure of merit. In 2017, a remarkable 6.5 W laser beam brightness figure of merit and 7.9 W/m^2 TEM$_{00}$-mode collection efficiency was obtained using a 4 mm diameter, 35 mm length Nd: YAG laser rod with a heliostat-parabolic mirror system [54]. In 2022, a small-size Ce: Nd: YAG solar-powered laser was studied. The Ce: Nd: YAG laser rod (2.5 mm diameter and 25 mm length) is end-side pumped by the concentrated solar radiation to enhance the laser efficiency and thermal performance significantly. For 249 W incoming solar power at an irradiance of 850 W/m^2, 11.2 W multimode solar laser power is achieved, corresponding to the solar-to-laser power conversion efficiency of 4.50%, the solar laser collection efficiency of 38.22 W/m^2, and slope efficiency of 6.8% [60]. The most efficient simultaneous emissions of three continuous-wave solar laser beams within a single conical pump cavity is also reported in year 2022. The presented system produces 16.5 W continuous-wave total multimode laser power, corresponding to 4.64% solar-to-laser conversion efficiency, 41.25 W/m^2 collection efficiency, and 7.64% slope efficiency [63].

6. Conclusions and perspectives

This article reviewed the significant progress of solar-powered solid-state lasers. We summarized the laser construction, working principle, energy mechanism, beam shaping, solar concentrators, different laser rods, and laser pumping schemes. From the survey of solar lasers, it is concluded that there are still several challenges in this research area, including the sun's position due to earth rotation, optical aberrations, low conversion efficiency, scattering and absorption losses, and thermal lens effect.

As the natural sunlight is insufficient for laser action, additional concentrating optics are necessary to collect and concentrate the solar radiations at the laser head. In solar lasers, parabolic mirrors and Fresnel lenses are used primarily. A parabolic mirror can collect and focus the entire wavelength range to a focal point without dispersion. However, the maximum output from the unit area of the parabolic concentrator is less. Fresnel lens has numerous advantages, such as being lightweight, low cost, and highly efficient for solar radiation collection. However, the Fresnel lens has chromatic aberration, reducing the focusing efficiency. A sun tracker is also employed in solar lasers to consider the sun's daily and seasonal movement. The tracking device increases the overall cost

of solar lasers. The laser material is heated by highly concentrated solar radiation, and then a coolant (water) is used to cool the material. Hence, a temperature difference is generated inside the laser cavity, causing the thermal lens effect that decreases the laser efficiency and the beam quality.

We believe that solar energy is a widely distributed clean energy and has great opportunities for research in terms of space and terrestrial applications. Since the solar laser's collection efficiency and output power depend on the concentrators, the freeform optics can improve the performance of solar lasers concomitantly by providing a large acceptance angle to the incident solar radiations. This will also maximize the focusing efficiency of solar concentrators by minimizing optical aberrations. The freeform concentrator would offer homogenous uniform irradiance distribution to the laser medium, which also helps to reduce the thermal lens effect to avoid beam distortion. The multirod solar laser beam technology and end-side (hybrid) pumping method could control the thermal lensing effect. It has been believed that more and more innovative research on solar concentrators (primary, secondary, and tertiary), laser rods, and the shape of pump cavities will be proposed in the future to overcome the present challenges.

Declaration of Competing Interest

The authors declare that they have no known competing financial interests or personal relationships that could have appeared to influence the work reported in this paper.

Data Availability

No data was used for the research described in the article.

Acknowledgement

References

[1] S. Krauter, Solar electric power generation, 10, Springer Berlin Heidelberg, Berlin, Heidelberg, 2006, p. 978. -973.

[2] P.D. Dongare, A. Alabastri, O. Neumann, P. Nordlander, N.J. Halas, Solar thermal desalination as a nonlinear optical process, Proc. Natl Acad. Sci. 116 (2019) 13182–13187.

[3] W.N.Y.M. Desa, A. Fudholi, Z. Yaakob, Energy-economic-environmental analysis of solar drying system: a review, Int. J. Power Electron. Drive Syst. 11 (2020) 1011.

[4] F. Trombe, Solar furnaces and their applications, Sol. Energy 1 (1957) 9–15.

[5] N. Panwar, S. Kaushik, S. Kothari, State of the art of solar cooking: An overview, Renewable Sustainable Energy Rev. 16 (2012) 3776–3785.

[6] S. Gorjian, F. Calise, K. Kant, M.S. Ahamed, B. Copertaro, G. Najafi, X. Zhang, M. Aghaei, R.R. Shamshiri, A review on opportunities for implementation of solar energy technologies in agricultural greenhouses, J. Cleaner Prod. 285 (2021), 124807.

[7] R. Shukla, K. Sumathy, P. Erickson, J. Gong, Recent advances in the solar water heating systems: A review, Renewable Sustainable Energy Rev. 19 (2013) 173–190.

[8] M.B. Hayat, D. Ali, K.C. Monyake, L. Alagha, N. Ahmed, Solar energy—A look into power generation, challenges, and a solar-powered future, Int. J. Energy Res. 43 (2019) 1049–1067.

[9] D. Graham-Rowe, Solar-powered lasers, Nat. Photonics 4 (2010) 64–65.

[10] A floating solar still to desalinate seawater. Available online at https://www.usgs.gov/media/images/a-floating-solar-still-to-desalinate-seawater (accessed on 1 March 2022). .

[11] S. Indora, T.C. Kandpal, Solar energy for institutional cooking in India: prospects and potential, Environ., Dev. Sustainability 22 (2020) 7153–7175.

[12] How fast can solar cars go? Available online at https://science.howstuffworks.com/science-vs-myth/everyday-myths/how-fast-can-solar-cars-go.htm(accessed on 30 November 2021).

[13] Solar Furnace, Operation and Uses. Available online athttps://solar-energy.technology/solar-thermal/solar-furnace (accessed on 30 December 2021).

[14] Solar Water Heaters. Available online at https://www.energy.gov/energysaver/solar-water-heaters (accessed on 28 November 2021).

[15] Cabinet Solar Dryer. Available online at http://seedngo.com/activities/c abinet-solar-dryer/(accessed on 28 November 2021).

[16] These images of the world's 'largest' solar power plant in India will leave you awestruck! Available online at https://www.financialexpress.com/photos/busin ess-gallery/536047/world-largest-solar-power-plant-adani-group-tamil-nadu-in dia-features-and-highlights/(accessed on 1 November 2021).

[17] T. Dinh, T. Ohkubo, T. Yabe, Development of solar concentrators for high-power solar-pumped lasers, Appl. Opt. 53 (2014) 2711–2719.

[18] Z. Guan, C. Zhao, S. Yang, Y. Wang, J. Ke, H. Zhang, Demonstration of a free-space optical communication system using a solar-pumped laser as signal transmitter, Laser Phys. Lett. 14 (2017), 055804.

[19] M. Vasile, C.A. Maddock, Design of a formation of solar pumped lasers for asteroid deflection, Adv. Space Res. 50 (2012) 891–905.

[20] S. Shen, X. Jin, C. Hao, Cleaning space debris with a space-based laser system, Chin. J. Aeronaut. 27 (2014) 805–811.

[21] T. Yabe, K. Yoshida, S. Uchida, Demonstrated fossil-fuel-free energy cycle using magnesium and laser, in: International Congress on Applications of Lasers & Electro-Optics, Laser Institute of America, 2007, p. M1103.

[22] T. Yabe, T. Ohkubo, S. Uchida, K. Yoshida, M. Nakatsuka, T. Funatsu, A. Mabuti, A. Oyama, K. Nakagawa, T. Oishi, High-efficiency and economical solar-energy-pumped laser with Fresnel lens and chromium codoped laser medium, Appl. Phys. Lett. 90 (2007), 261120.

[23] T. Masuda, M. Iyoda, Y. Yasumatsu, S. Dottermusch, I.A. Howard, B.S. Richards, J.-F. Bisson, M. Endo, A fully planar solar pumped laser based on a luminescent solar collector, Commun. Phys. 3 (2020) 1–6.

[24] T. Maiman, Stimulated optical radiation in ruby, in: A Century of Nature, 2010, University of Chicago Press, 1960, pp. 113–114.

[25] D. Liang, J. Almeida, Highly efficient solar-pumped Nd: YAG laser, Opt. Express 19 (2011) 26399–26405.

[26] Z. Kiss, H. Lewis, R. Duncan Jr, Sun pumped continuous optical maser, Appl. Phys. Lett. 2 (1963) 93–94.

[27] J.D. Cox, U.H. Kurzweg, N.H. Weinstein, R.T. Schneider, Research on solar pumped liquid lasers, in, 1985.

[28] A.A. Seregin, E.A. Seregina, Model of a pulsed liquid solar-pumped spaceborne laser, Quantum Electron. 34 (2004) 99.

[29] S. Payziyev, S. Bakhramov, F. Shayimov, Enhancing of solar pumped liquid laser efficiency, Appl. Solar Energy 52 (2016) 68–71.

[30] H. ARASHI, A solar-pumped laser for space use, The J. Space Technol. Sci. 1 (1985) 2 23-22 31.

[31] W. Christiansen, A new concept for solar pumped lasers, Prog. Astronaut. Aeronaut. 61 (1978) 346–356.

[32] O. Yesil, W.H. Christiansen, Optically pumped carbon dioxide laser mixtures (using solar radiation), J. Energy 3 (1979) 315–318.

[33] J.H. Lee, W.R. Weaver, A solar simulator-pumped atomic iodine laser, Appl. Phys. Lett. 39 (1981) 137–139.

[34] R.J. Insuik, W.H. Christiansen, Blackbody-pumped CO2 laser experiment, AIAA J. 22 (1984) 1271–1274.

[35] O. Danilov, A. Zhevlakov, M. Yur'ev, Optically (solar) pumped oxygen-iodine lasers, Opt. Spectrosc. 117 (2014) 145–151.

[36] Properties of Solid-State Laser Materials, DOI https://doi.org/10.1007/978-3-662-15143-3_2.

[37] C. Young, A sun-pumped cw one-watt laser, Appl. Opt. 5 (1966) 993–997.

[38] H. Arashi, Y. Oka, N. Sasahara, A. Kaimai, M. Ishigame, A solar-pumped cw 18 W Nd: YAG laser, Japan. J. Appl. Phys. 23 (1984) 1051.

[39] D. Liang, C.R. Vistas, J. Almeida, B.D. Tibúrcio, D. Garcia, Side-pumped continuous-wave Nd: YAG solar laser with 5.4% slope efficiency, Sol. Energy Mater. Sol. Cells 192 (2019) 147–153.

[40] T. Kato, H. Ito, K. Hasegawa, T. Ichikawa, A. Ikesue, S. Mizuno, Y. Takeda, A. Ichiki, T. Motohiro, Effect of Cr content on the output of a solar-pumped laser employing a Cr-doped Nd: YAG ceramic laser medium operating in sunlight, Japan. J. Appl. Phys. 58 (2019), 062007.

[41] H. Costa, J. Almeida, D. Liang, B.D. Tibúrcio, D. Garcia, M. Catela, C.R. Vistas, Quasi-Gaussian Multibeam Solar Laser Station for a Megawatt Solar Furnace, J. Solar Energy Res. Updates 8 (2021) 11–20.

[42] C.R. Vistas, D. Liang, J. Almeida, Solar-pumped TEM00 mode laser simple design with a grooved Nd: YAG rod, Sol. Energy 122 (2015) 1325–1333.

[43] M. Endo, Optical characteristics of Cr3+ and Nd3+ codoped Y3Al5O12 ceramics, Opt. Laser Technol. 42 (2010) 610–616.

[44] I.-H. Hwang, J.-H. Lee, Efficiency and threshold pump intensity of cw solar-pumped solid-state lasers, IEEE J. Quantum Electron. 27 (1991) 2129–2134.

[45] T. Dinh, T. Ohkubo, T. Yabe, H. Kuboyama, 120 watt continuous wave solar-pumped laser with a liquid light-guide lens and an Nd: YAG rod, Opt. Lett. 37 (2012) 2670–2672.

[46] D. Liang, J. Almeida, D. Garcia, Comparative study of Cr: Nd: YAG and Nd: YAG solar laser performances, in: 8th Iberoamerican Optics Meeting and 11th Latin American Meeting on Optics, Lasers, and Applications, SPIE, 2013, pp. 973–979.

[47] M. Lando, Y. Shimony, R.M. Benmair, D. Abramovich, V. Krupkin, A. Yogev, Visible solar-pumped lasers, Opt. Mater. 13 (1999) 111–115.

[48] H. Yagi, T. Yanagitani, H. Yoshida, M. Nakatsuka, K. Ueda, The optical properties and laser characteristics of Cr3+ and Nd3+ co-doped Y3Al5O12 ceramics, Opt. Laser Technol. 39 (2007) 1295–1300.

[49] K. Fujioka, T. Saiki, S. Motokoshi, Y. Fujimoto, H. Fujita, M. Nakatsuka, Parameter mapping survey on optimized sensitizing effect of Ce/Cr/Nd: YAG material for solar-pumped solid-state lasers, J. Lumin. 143 (2013) 10–13.

[50] S. Payziyev, K. Makhmudov, Y.A. Abdel-Hadi, Simulation of a new solar Ce: Nd: YAG laser system, Optik 156 (2018) 891–895.

[51] T. Kato, H. Ito, K. Hasegawa, T. Ichikawa, A. Ikesue, S. Mizuno, Y. Takeda, A. Ichiki, T. Motohiro, Energy transfer efficiency from Cr3+ to Nd3+ in Cr, Nd YAG ceramics laser media in a solar-pumped laser in operation outdoors, Opt. Mater. 110 (2020), 110481.

[52] D. Liang, J. Almeida, E. Guillot, Side-pumped continuous-wave Cr: Nd: YAG ceramic solar laser, Appl. Phys. B 111 (2013) 305–311.

[53] D. Liang, C.R. Vistas, B.D. Tibúrcio, J. Almeida, Solar-pumped Cr: Nd: YAG ceramic laser with 6.7% slope efficiency, Sol. Energy Mater. Sol. Cells 185 (2018) 75–79.

[54] D. Liang, J. Almeida, C.R. Vistas, E. Guillot, Solar-pumped Nd: YAG laser with 31.5 W/m2 multimode and 7.9 W/m2 TEM00-mode collection efficiencies, Sol. Energy Mater. Sol. Cells 159 (2017) 435–439.

[55] W. Holloway, M. Kestigian, Optical properties of cerium-activated garnet crystals, JOSA 59 (1969) 60–63.

[56] J. Mares, B. Jacquier, C. Pedrini, G. Boulon, Energy transfer mechanisms between Ce3+ and Nd3+ in YAG: Nd, Ce at low temperature, Revue de physique appliquée 22 (1987) 145–152.

[57] Y. Tai, G. Zheng, H. Wang, J. Bai, Near-infrared quantum cutting of Ce3+–Nd3+ co-doped Y3Al5O12 crystal for crystalline silicon solar cells, J. Photochem. Photobiol. A 303 (2015) 80–85.

[58] J.X. Meng, J.Q. Li, Z.P. Shi, K.W. Cheah, Efficient energy transfer for Ce to Nd in Nd/ Ce codoped yttrium aluminum garnet, Appl. Phys. Lett. 93 (2008) 221908.

[59] C.R. Vistas, D. Liang, D. Garcia, M. Catela, B.D. Tibúrcio, E. Guillot, J. Almeida, Uniform and Non-Uniform Pumping Effect on Ce: Nd: YAG Side-Pumped Solar Laser Output Performance, Energies 15 (2022) 3577.

[60] D. Garcia, D. Liang, C.R. Vistas, H. Costa, M. Catela, B.D. Tibúrcio, J. Almeida, Ce: Nd: YAG Solar Laser with 4.5% Solar-to-Laser Conversion Efficiency, Energies 15 (2022) 5292.

[61] C.R. Vistas, D. Liang, D. Garcia, J. Almeida, B.D. Tiburcio, E. Guillot, Ce: Nd: YAG continuous-wave solar-pumped laser, Optik 207 (2020), 163795.

[62] C.R. Vistas, D. Liang, J. Almeida, B.D. Tibúrcio, D. Garcia, M. Catela, H. Costa, E. Guillot, Ce: Nd: YAG side-pumped solar laser, J. Photonics Energy 11 (2021), 018001.

[63] D. Liang, C.R. Vistas, D. Garcia, B.D. Tibúrcio, M. Catela, H. Costa, E. Guillot, J. Almeida, Most efficient simultaneous solar laser emissions from three Ce: Nd: YAG rods within a single pump cavity, Sol. Energy Mater. Sol. Cells 246 (2022), 111921.

[64] J. Almeida, D. Liang, D. Garcia, B.D. Tibúrcio, H. Costa, M. Catela, E. Guillot, C. R. Vistas, 40 W Continuous Wave Ce: Nd: YAG Solar Laser through a Fused Silica Light Guide, Energies 15 (2022) 3998.

[65] A. Kaminskij, K.S. Bagdasarov, G. Bogomolova, M. Gritsenko, A. Kevorkov, S. Sarkisov, Luminescence and stimulated emission of Nd 3+ ions in Gd 3 Sc 2 Ga 3 O 12 crystals, Phys. Status Solidi A 34 (1976) K109–K114.

[66] M. Weksler, J. Shwartz, Solar-pumped solid-state lasers, IEEE J. Quantum Electron. 24 (1988) 1222–1228.

[67] Y. Noter, M. Oron, J. Shwartz, M. Weksler, A. Yogev, Solar Pumped Nd: Cr: GSGG Laser, in: 6th Mtg in Israel on Optical Engineering, SPIE, 1989, pp. 512–520.

[68] M. Endo, Feasibility study of a conical-toroidal mirror resonator for solar-pumped thin-disk lasers, Opt. Express 15 (2007) 5482–5493.

[69] W.F. Coleman, Lasers-An introduction, ACS Publications, 1982.

[70] A. Einstein, Phys. Zeit. 18 (1917) 121.

[71] O. Svelto, D.C. Hanna, Principles of lasers, Springer, 1998.

[72] R.A. Dunlap, Lasers and Their Application to the Observation of Bose-Einstein Condensates, Morgan & Claypool Publishers, 2019.

[73] J.I.L. Almeida, Advances in solar-pumped laser efficiency and brightness, Universidade NOVA de Lisboa (Portugal), 2017 in.

[74] P. Laporta, V. Magni, O. Svelto, Comparative study of the optical pumping efficiency in solid-state lasers, IEEE J. Quantum Electron. 21 (1985) 1211–1218.

[75] Y.A. Abdel-Hadi, Simulation model of a new solar pumped laser system of Fresnel lens in Helwan of Egypt, NRIAG Journal of Astronomy and Geophysics 1 (2012) 195–198.

[76] A. Golger, I. Klimovskiĭ, Lasers pumped by solar radiation, Sov. J. Quantum Electron. 14 (1984) 164.

[77] M. Lando, D.G. Jenkins, H. Bernstein, J.J. O'Gallagher, R. Winston, A. Lewandowski, High-brightness-solar-pumped Nd: YAG laser design, in: 9th Meeting on Optical Engineering in Israel, SPIE, 1995, pp. 478–490.

[78] F.M. Dickey, Laser beam shaping: theory and techniques, CRC press, 2018.

[79] D.L. Shealy, J.A. Hoffnagle, Laser beam shaping profiles and propagation, Appl. Opt. 45 (2006) 5118–5131.

[80] F.M. Dickey, L.S. Weichman, R.N. Shagam, Laser beam shaping techniques. High-Power Laser Ablation III, SPIE, 2000, pp. 338–348.

[81] M. Duocastella, C.B. Arnold, Bessel and annular beams for materials processing, Laser Photonics Rev. 6 (2012) 607–621.

[82] R. Grojean, D. Feldman, J. Roach, Production of flat top beam profiles for high energy lasers, Rev. Sci. Instrum. 51 (1980) 375–376.

[83] J.A. Hoffnagle, C.M. Jefferson, Design and performance of a refractive optical system that converts a Gaussian to a flattop beam, Appl. Opt. 39 (2000) 5488–5499.

[84] G. Račiukaitis, E. Stankevičius, P. Gečys, M. Gedvilas, C. Bischoff, E. Jäger, U. Umhofer, F. Völklein, Laser Processing by Using Diffractive Optical Laser Beam Shaping Technique, J. Laser Micro/Nanoeng. (2011) 6.

[85] Z. Feng, B.D. Froese, R. Liang, D. Cheng, Y. Wang, Simplified freeform optics design for complicated laser beam shaping, Appl. Opt. 56 (2017) 9308–9314.

[86] S. Berwal, N. Khatri, Design and comparative analysis of fiber-coupled laser diode system using ball, cylindrical, and toroidal lens. High Power Lasers and Applications, SPIE, 2021, pp. 80–87.

[87] M. Rioux, R. Tremblay, P.-A. Belanger, Linear, annular, and radial focusing with axicons and applications to laser machining, Appl. Opt. 17 (1978) 1532–1536.

[88] M. Okida, Y. Hayashi, T. Omatsu, J. Hamazaki, R. Morita, Characterization of 1.06 μm optical vortex laser based on a side-pumped Nd: GdVO4 bounce oscillator, Appl. Phys. B 95 (2009) 69–73.

[89] I.A. Litvin, S. Ngcobo, D. Naidoo, K. Ait-Ameur, A. Forbes, Doughnut laser beam as an incoherent superposition of two petal beams, Opt. Lett. 39 (2014) 704–707.

[90] T.Y. Cherezova, S. Chesnokov, L. Kaptsov, A. Kudryashov, Doughnut-like laser beam output formation by intracavity flexible controlled mirror, Opt. Express 3 (1998) 180–189.

[91] C.R. Vistas, D. Liang, J. Almeida, B.D. Tibúrcio, D. Garcia, A doughnut-shaped Nd: YAG solar laser beam with 4.5 W/m2 collection efficiency, Sol. Energy 182 (2019) 42–47.

[92] J. Almeida, D. Liang, C. Vistas, A doughnut-shaped Nd: YAG solar laser beam, Opt. Laser Technol. 106 (2018) 1–6.

[93] M. Catela, D. Liang, C.R. Vistas, D. Garcia, B.D. Tibúrcio, H. Costa, J. Almeida, Doughnut-Shaped and Top Hat Solar Laser Beams Numerical Analysis, Energies 14 (2021) 7102.

[94] D. Jenkins, M. Lando, J. O'Gallagher, R. Winston, A solar-pumped Nd: YAG laser with a record efficiency of 4.7 watt/m 2, Bull. ISR. Phys. Soc 42 (1996) 101.

[95] M. Lando, J. Kagan, B. Linyekin, V. Dobrusin, A solar-pumped Nd: YAG laser in the high collection efficiency regime, Optics Communications 222 (2003) 371–381.

[96] T. Ohkubo, T. Yabe, K. Yoshida, S. Uchida, T. Funatsu, B. Bagheri, T. Oishi, K. Daito, M. Ishioka, Y. Nakayama, Solar-pumped 80 W laser irradiated by a Fresnel lens, Opt. Lett. 34 (2009) 175–177.

[97] D. Liang, J. Almeida, Design of ultrahigh brightness solar-pumped disk laser, Appl. Opt. 51 (2012) 6382–6388.

[98] D. Liang, J. Almeida, Solar-pumped TEM 00 mode Nd: YAG laser, Opt. Express 21 (2013) 25107–25112.

[99] P. Xu, S. Yang, C. Zhao, Z. Guan, H. Wang, Y. Zhang, H. Zhang, T. He, High-efficiency solar-pumped laser with a grooved Nd: YAG rod, Appl. Opt. 53 (2014) 3941–3944.

[100] P.D. Reusswig, S. Nechayev, J.M. Scherer, G.W. Hwang, M.G. Bawendi, M. Baldo, C. Rotschild, A path to practical solar pumped lasers via radiative energy transfer, Sci. Rep. 5 (2015) 1–6.

[101] S. Payziyev, K. Makhmudov, Solar pumped Nd: YAG laser efficiency enhancement using Cr: LiCAF frequency down-shifter, Optics Communications 380 (2016) 57–60.

[102] T. Masuda, M. Iyoda, Y. Yasumatsu, M. Endo, Low-concentrated solar-pumped laser via transverse excitation fiber-laser geometry, Opt. Lett. 42 (2017) 3427–3430.

[103] B. Villars, E.S. Hill, C.G. Durfee, Design and development of a high-power LED-pumped Ce: Nd: YAG laser, Opt. Lett. 40 (2015) 3049–3052.

[104] T. Masuda, S. Dottermusch, I. Howard, B. Richards, J. Bisson, M. Endo, Solar powered fiber laser for energy conversion applications. CLEO: Applications and Technology, Optical Society of America, 2020, p. AF3N, 4.

[105] S. Dottermusch, T. Masuda, M. Endo, B.S. Richards, I.A. Howard, Solar Pumping of Fiber Lasers with Solid-State Luminescent Concentrators: Design Optimization by Ray Tracing, Adv. Opt. Mater. 9 (2021) 2100479.

[106] B. Tibúrcio, D. Liang, J. Almeida, D. Garcia, C. Vistas, Dual-rod pumping concept for TEM 00-mode solar lasers, Appl. Opt. 58 (2019) 3438–3446.

[107] J. Almeida, D. Liang, B.D. Tibúrcio, D. Garcia, C.R. Vistas, Numerical modeling of a four-rod pumping scheme for improving TEM00-mode solar laser performance, J. Photonics Energy 9 (2019), 018001.

[108] D. Liang, J. Almeida, D. Garcia, B.D. Tibúrcio, E. Guillot, C.R. Vistas, Simultaneous solar laser emissions from three Nd: YAG rods within a single pump cavity, Sol. Energy 199 (2020) 192–197.

[109] H. Costa, J. Almeida, D. Liang, D. Garcia, M. Catela, B.D. Tibúrcio, C.R. Vistas, Design of a multibeam solar laser station for a megawatt solar furnace, Opt. Eng. 59 (2020), 086103.

[110] J. Almeida, D. Liang, H. Costa, D. Garcia, B.D. Tibúrcio, M. Catela, C.R. Vistas, Seven-rod pumping concept for simultaneous emission of seven TEM00-mode solar laser beams, J. Photonics Energy 10 (2020), 038001.

[111] D. Liang, J. Almeida, B.D. Tibúrcio, M. Catela, D. Garcia, H. Costa, C.R. Vistas, Seven-rod pumping approach for the most efficient production of TEM00 mode solar laser power by a Fresnel lens, J. Sol. Energy Eng. (2021) 143.

[112] D. Liang, J. Almeida, C.R. Vistas, M. Oliveira, F. Gonçalves, E. Guillot, High-efficiency solar-pumped TEM00-mode Nd: YAG laser, Sol. Energy Mater. Sol. Cells 145 (2016) 397–402.

[113] H. Costa, J. Almeida, D. Liang, M. Catela, D. Garcia, B.D. Tibúrcio, C.R. Vistas, Zigzag Multirod Laser Beam Merging Approach for Brighter TEM00-Mode Solar Laser Emission from a Megawatt Solar Furnace, Energies 14 (2021) 5437.

[114] S. Mehellou, A. Beggas, N. Hamrouni, F. Rehouma, The Effects of the Pumping Configurations on TEM00 Mode Nd: YAG Solar Laser Performance: a Review, Braz. J. Phys. 52 (2022) 1–26.

[115] B. Tibúrcio, D. Liang, J. Almeida, D. Garcia, M. Catela, H. Costa, C. Vistas, Tracking error compensation capacity measurement of a dual-rod side-pumping solar laser, Renewable Energy 195 (2022) 1253–1261.

[116] J. Almeida, D. Liang, E. Guillot, Improvement in solar-pumped Nd: YAG laser beam brightness, Opt. Laser Technol. 44 (2012) 2115–2119.

[117] J. Almeida, D. Liang, E. Guillot, Y. Abdel-Hadi, A 40 W cw Nd: YAG solar laser pumped through a heliostat: a parabolic mirror system, Laser Phys. 23 (2013), 065801.

[118] J. Almeida, D. Liang, Design of TEM00 mode side-pumped Nd: YAG solar laser, Optics Communications 333 (2014) 219–225.

[119] D. Liang, J. Almeida, C.R. Vistas, Scalable pumping approach for extracting the maximum TEM 00 solar laser power, Appl. Opt. 53 (2014) 7129–7137.

[120] J. Almeida, D. Liang, C. Vistas, E. Guillot, Highly efficient end-side-pumped Nd: YAG solar laser by a heliostat–parabolic mirror system, Appl. Opt. 54 (2015) 1970–1977.

[121] J. Almeida, D. Liang, C. Vistas, R. Bouadjemine, E. Guillot, 5.5 W continuous-wave TEM00-mode Nd: YAG solar laser by a light-guide/2V-shaped pump cavity, Appl. Phys. B 121 (2015) 473–482.

[122] D. Liang, J. Almeida, C.R. Vistas, E. Guillot, Solar-pumped TEM00 mode Nd: YAG laser by a heliostat—Parabolic mirror system, Sol. Energy Mater. Sol. Cells 134 (2015) 305–308.

[123] D. Liang, J. Almeida, C. Vistas, 25 W/m 2 collection efficiency solar-pumped Nd: YAG laser by a heliostat-parabolic mirror system, Appl. Opt. 55 (2016) 7712–7717.

[124] M. Oliveira, D. Liang, J. Almeida, C.R. Vistas, F. Gonçalves, R. Martins, A path to renewable Mg reduction from MgO by a continuous-wave Cr: Nd: YAG ceramic solar laser, Sol. Energy Mater. Sol. Cells 155 (2016) 430–435.

[125] R. Bouadjemine, D. Liang, J. Almeida, S. Mehellou, C. Vistas, A. Kellou, E. Guillot, Stable solar-pumped Nd: YAG laser operation by a twisted fused silica light-guide, Opt. Laser Technol. 97 (2017) 1–11.

[126] S. Mehellou, D. Liang, J. Almeida, R. Bouadjemine, C.R. Vistas, E. Guillot, F. Rehouma, Stable solar-pumped TEM00-mode 1064 nm laser emission by a monolithic fused silica twisted light guide, Sol. Energy 155 (2017) 1059–1071.

[127] Z. Guan, C. Zhao, J. Li, D. He, H. Zhang, 32.1 W/m2 continuous wave solar-pumped laser with a bonding Nd: YAG/YAG rod and a Fresnel lens, Opt. Laser Technol. 107 (2018) 158–161.

[128] A.B. Meinel, M.P. Meinel, Physics Looks at Solar Energy, Phys. Today 25 (1972) 44–50.

[129] R. Winston, Principles of solar concentrators of a novel design, Sol. Energy 16 (1974) 89–95.

[130] F. Muhammad-Sukki, R. Ramirez-Iniguez, S.G. McMeekin, B.G. Stewart, B. Clive, Solar concentrators, Int. J. Appl. Sci. 1 (2010) 1–15.

[131] R. Leutz, A. Suzuki, Nonimaging Fresnel lenses: design and performance of solar concentrators, Springer Science & Business Media, 2001.

[132] G. Tiwari, A. Atheaya, A. Tiwari, Review on Solar Thermal Power Concentrators, Open Acc. J. Photoen. 1 (2017) 00016.

[133] D. Freier, R. Ramirez-Iniguez, T. Jafry, F. Muhammad-Sukki, C. Gamio, A review of optical concentrators for portable solar photovoltaic systems for developing countries, Renewable Sustainable Energy Rev. 90 (2018) 957–968.

[134] R. Winston, J.C. Miñano, P.G. Benitez, Nonimaging optics, Elsevier, 2005.

[135] A. Dang, Concentrators: a review, Energy Convers. Manage. 26 (1986) 11–26.

[136] J. Yellowhair, P. Apostolopoulos, D.E. Small, D.K. Novick, M.S. Mann, Development of an Aerial Imaging System for Heliostat Canting Assessments, Sandia National Lab.(SNL-NM), Albuquerque, NMUnited States, 2020.

[137] A. Rabl, Comparison of solar concentrators, Argonne National Lab., Ill.(USA, 1975.

[138] K. Lovegrove, J. Pye, Fundamental principles of concentrating solar power systems. Concentrating Solar Power Technology, Elsevier, 2021, pp. 19–71.

[139] W. Xie, Y. Dai, R. Wang, K. Sumathy, Concentrated solar energy applications using Fresnel lenses: A review, Renewable Sustainable Energy Rev. 15 (2011) 2588–2606.

[140] O. Miller, J. McLeod, W. Sherwood, Thin sheet plastic Fresnel lenses of high aperture, JOSA 41 (1951) 807–815.

[141] R. Leutz, A. Suzuki, A. Akisawa, T. Kashiwagi, Design of a nonimaging Fresnel lens for solar concentrators, Sol. Energy 65 (1999) 379–387.

[142] B. Tibúrcio, D. Liang, J. Almeida, D. Garcia, M. Catela, H. Costa, C. Vistas, Improving side-pumped solar lasers using ring-array concentrators, Int. J. Sustainable Energy 41 (2022) 868–888.

[143] R. Matos, D. Liang, J. Almeida, B. Tibúrcio, C. Vistas, High-efficiency solar laser pumping by a modified ring-array concentrator, Opt. Commun. 420 (2018) 6–13.

[144] D. Garcia, D. Liang, B. Tibúrcio, J. Almeida, C. Vistas, A three-dimensional ring-array concentrator solar furnace, Sol. Energy 193 (2019) 915–928.

[145] D. Garcia, D. Liang, J. Almeida, B.D. Tibúrcio, H. Costa, M. Catela, C.R. Vistas, Analytical and numerical analysis of a ring-array concentrator, Int. J. Energy Res. 45 (2021) 15110–15123.

[146] B.D. Tibúrcio, D. Liang, J. Almeida, R. Matos, C.R. Vistas, Improving solar-pumped laser efficiency by a ring-array concentrator, J. Photonics Energy 8 (2018), 018002.

[147] G. AM, The Pyreheliophoro, INPI, France, 1899.

[148] M. Mouzouris, M.J. Brooks, Nonimaging solar thermal collector for high temperature terrestrial and space applications. Nonimaging Optics: Efficient Design for Illumination and Solar Concentration VI, SPIE, 2009, pp. 120–131.

[149] V. Vasylyev, O. Tovmachenko, S. Vasylyev, Expected Optical Performance of Novel Type Multi-Element High-Heat Solar Concentrators, in: PROCEEDINGS OF THE SOLAR CONFERENCE, Citeseer, 2002, pp. 213–216.

[150] H. Hinterberger, R. Winston, Efficient light coupler for threshold Čerenkov counters, Rev. Sci. Instrum. 37 (1966) 1094–1095.

[151] V. Baranov, G. Melnikov, Study of the illumination characteristics of hollow focons, Sov. J. Opt. Technol 33 (1966) 408–411.

[152] R. Winston, H. Hinterberger, Principles of cylindrical concentrators for solar energy, Sol. Energy 17 (1975) 255–258.

[153] A. Rabl, R. Winston, Ideal concentrators for finite sources and restricted exit angles, Appl. Opt. 15 (1976) 2880–2883.

[154] A. Rabl, N. Goodman, R. Winston, Practical design considerations for CPC solar collectors, Sol. Energy 22 (1979) 373–381.

[155] X. Ning, R. Winston, J. O'Gallagher, Dielectric totally internally reflecting concentrators, Appl. Opt. 26 (1987) 300–305.

[156] J. Geusic, H. Marcos, L. Van Uitert, Laser oscillations in Nd-doped yttrium aluminum, yttrium gallium and gadolinium garnets, Appl. Phys. Lett. 4 (1964) 182–184.

[157] V. Bachmann, C. Ronda, A. Meijerink, Temperature quenching of yellow Ce3+ luminescence in YAG: Ce, Chem. Mater. 21 (2009) 2077–2084.

[158] K. Johnson, S. Selkowitz, Light guide design principles, Lawrence Berkeley National Lab.(LBNL), Berkeley, CAUnited States, 1986.

[159] J. Spear, Transmittance Measurements of Hollow Reflecting Light Guide. Unpublished Report, Lawrence Berkeley Laboratory, 1986.

[160] L. Whitehead, R. Nodwell, F. Curzon, New efficient light guide for interior illumination, Appl. Opt. 21 (1982) 2755–2757.

[161] L.A. Whitehead, D.N. Brown, R.A. Nodwell, A new device for distributing concentrated sunlight in building interiors, Energy Build. 6 (1984) 119–125.

[162] J. Cariou, J. Dugas, L. Martin, Transport of solar energy with optical fibres, Sol. Energy 29 (1982) 397–406.

[163] L. Fraas, W. Pyle, P. Ryason, Concentrated and piped sunlight for indoor illumination, Appl. Opt. 22 (1983) 578–582.

[164] M. Duguay, R. Edgar, Lighting with sunlight using sun tracking concentrators, Appl. Opt. 16 (1977) 1444–1446.

[165] M.A. Duguay, G. Aumiller, Transmission of 3-D images by means of lens guides, Appl. Opt. 18 (1979) 2081–2084.

[166] C. Vistas, D. Liang, D. Garcia, B. Tibúrcio, J. Almeida, 32 W TEM00-Mode Side-Pumped Solar Laser Design, Appl. Solar Energy 56 (2020) 449–457.

[167] D. Volk, Conoid refracting surfaces and conoid lenses, Am. J. Ophthalmol. 46 (1958) 86–95.

[168] A. Sonnefeld, Veb Carl Zeiss, Jena: Golden Jubilee of Work on Aids to Vision (1962).

[169] US4181409A - Aspheric lens series - Google Patents.

[170] J. Sasián, Introduction to lens design, Cambridge University Press, 2019.

[171] D. Adams, S. Ament, Understanding Aspheric Lenses: Key specifications and their impact on performance, Optik Photonik 13 (2018) 60–63.

[172] Y. Gao, X.-f. Liu, C. Sun, Y.-z. Huang, B. Li, The experimental investigation of Nd: YAG grooved rods' thermal focal distance, Laser J. 29 (2008) 6–7.

[173] S. Payziyev, K. Makhmudov, A Simple Multi-Pass Side-Pumping Scheme for Solar Powered Lasers, Recent Adv. Photonics Opt. 2 (2019) 31–35.

[174] S. Mehellou, F. Rehouma, N. Hamrouni, L. Bouras, Thermal loading effects on Nd: YAG solar-laser performance in end-pumping and side-pumping configurations: a review, Opt. Eng. 57 (2018), 120902.

[175] S. Chénais, F. Druon, S. Forget, F. Balembois, P. Georges, On thermal effects in solid-state lasers: The case of ytterbium-doped materials, Prog. Quantum Electron. 30 (2006) 89–153.

[176] M.S. El-Daher, Finite element analysis of thermal effects in diode end-pumped solid-state lasers, Adv. Opt. Technol. (2017) 2017.